SEVIRI Water Turbidity

Advanced Theoretical Basis Document

Deliverable D3.1

Issue 1.5

2 March 2016

Prepared by

Kevin Ruddick, Quinten Vanhellemont, Bouchra Nechad and the SEVIRI-WT Project team

Table of Contents

ACRONYMS AND ABBREVIATIONS **4**

REFERENCES **5**

1 SCOPE OF THIS DOCUMENT **7**

2 CHANGE LOG **7**

3 INTRODUCTION **9**

4 PIXEL IDENTIFICATION **11**

4.1 ALGORITHM DESCRIPTION 11
4.2 ALGORITHM VALIDATION 12
4.3 UNCERTAINTIES 12
4.4 QUALITY FLAGGING 13
4.5 ADAPTATION TO DIFFERENT SEVIRI SENSORS 13
4.6 ALGORITHM LIMITATIONS AND RECOMMENDATIONS FOR FUTURE IMPROVEMENTS 13

5 ATMOSPHERIC CORRECTION **13**

5.1 ALGORITHM DESCRIPTION 14
5.1.1 Absorbing gas and Rayleigh correction *15*
5.1.2 Aerosol correction *15*
5.2 ALGORITHM VALIDATION 30
5.3 UNCERTAINTIES 30
5.4 QUALITY FLAGGING 30
5.5 ADAPTATION TO DIFFERENT SEVIRI SENSORS 30
5.6 ALGORITHM LIMITATIONS AND RECOMMENDATIONS FOR FUTURE IMPROVEMENTS 30

6 STANDARDISATION OF WATER REFLECTANCE PRODUCTS **31**

6.1 BAND-SHIFTING 31
6.1.1 Method for analysing narrow band approach *33*
5.1.2. Results for uncertainty of standardised narrow band approach *34*
6.1.2 Results for uncertainty of standardised narrow band approach *36*
6.1.3 Implementation *36*
6.2 TEMPORAL FILTERING 36
6.3 BIDIRECTIONAL EFFECTS 37
6.4 SUMMARY OF STANDARDISATION OF REFLECTANCE PRODUCTS 37

7 WATER REFLECTANCES AT HRV BAND SPATIAL RESOLUTION **38**

7.1 EFFECTIVE ATMOSPHERIC TRANSMITTANCE AT HRV BAND 38
7.2 CONVERTING HRV BAND TO VIS0.6 AND VIS0.8 BANDS 39
7.2.1 Converting HRV to VIS0.6 and VIS0.8 reflectance – linear approach *39*
7.2.2 Converting HRV to VIS0.6 and VIS0.8 reflectance – non-linear approach *39*
7.2.3 Converting HRV to VIS0.6 and VIS0.8 reflectance – locally-linear approach *40*
7.3 HRV-SHARPENING – SUMMARY OF PROPOSED IMPLEMENTATION 41

8 SUSPENDED MATTER-RELATED WATER PRODUCTS (L2W/S) **43**

8.1 TURBIDITY (T) 44
8.1.1 T Algorithm description *44*
8.1.2 T Algorithm for HRV band *48*

8.1.3 T Algorithm validation 48
8.1.4 T Uncertainties 50
8.1.5 T Quality flagging 50
8.1.6 T algorithm adaptation to different SEVIRI sensors 50
8.1.7 T algorithm limitations and recommendations for future improvements 50
8.2 SUSPENDED PARTICULATE MATTER (SPM) 50
8.2.1 SPM Algorithm description 50
8.2.2 SPM Algorithm for HRV band 50
8.2.3 SPM Algorithm validation 50
8.2.4 SPM Uncertainties 51
8.2.5 SPM Quality flagging 51
8.2.6 SPM algorithm adaptation to different SEVIRI sensors 51
8.2.7 SPM algorithm limitations and recommendations for future improvements 51
8.3 PARTICULATE BACKSCATTER (BBP640) 51
8.3.1 bbp640 Algorithm description 51
8.3.2 bbp640 Algorithm for HRV band 51
8.3.3 bbp640 Algorithm validation 51
8.3.4 bbp640 Uncertainties 51
8.3.5 bbp640 Quality flagging 52
8.3.6 bbp640 algorithm adaptation to different SEVIRI sensors 52
8.3.7 bbp640 algorithm limitations and recommendations for future improvements 52
9 ATTENUTATION-RELATED PRODUCTS (L2W/K) 52
9.1.1 Diffuse attenuation of PAR 52
9.1.2 Euphotic depth 52
9.1.3 Secchi depth 53
10 OTHER L2W FLAG PRODUCTS 53
10.1.1 Coccolithophore bloom flag 53
10.1.2 Extreme high biomass bloom flag 53
10.1.3 Extreme cyanobacteria bloom or surface scum flag 53
11 CONCLUSIONS AND RECOMMENDATIONS 54
ANNEX A SEMI-ANALYTICAL REFLECTANCE MODEL 55

Acronyms and Abbreviations

ATBD	Advanced Theoretical Basis Document
BC	Brockmann Consult GmbH
LR	Low Resolution (product grid)
HR	High Resolution (product grid)
HRV	High Resolution Visible (band)
OC	Ocean Colour
PDD	Product Definition Document
PQR	Product Quality and Validation Report
RBINS	Royal Belgium Institute for Natural Sciences
TSM	Total Suspended Matter
URD	User Requirements Document
XTW	eXtremely Turbid Waters

References

Babin, M., A. Morel, V. Fournier-Sicre, F. Fell, and D. Stramski. 2003. “Light Scattering Properties of Marine Particles in Coastal and Open Ocean Waters as Related to the Particle Mass Concentration.” *Limnology and Oceanography* 28 (2): 843–59.

Devlin, M.J., J. Barry, D.K. Mills, R.J. Gowen, J. Foden, D. Sivyer, and P. Tett. 2008. “Relationships between Suspended Particulate Material, Light Attenuation and Secchi Depth in UK Marine Waters.” *Estuarine, Coastal and Shelf Science* 79: 429–39.

Doerffer, R. 2006. “How to Determine IOPs from MERIS Data.” In *Second Working Meeting on MERIS and AATSR Calibration and Geophysical Validation (MAVT-2006)*, edited by D. Danesy. Vol. SP-615. ESA.

Dogliotti, A.I., K.G. Ruddick, B. Nechad, D. Doxaran, and E. Knaeps. 2015. “A Single Algorithm to Retrieve Turbidity from Remotely-Sensed Data in All Coastal and Estuarine Waters.” *Remote Sensing of Environment* 156 (0): 157–68. doi:10.1016/j.rse.2014.09.020.

Doron, M., S. Bélanger, D. Doxaran, and M. Babin. 2011. “Spectral Variations in the near-Infrared Ocean Reflectance.” *Remote Sens. Environ.* 15: 1617–31.

Gordon, H.R., O.B. Brown, R.H. Evans, J.W. Brown, R.C. Smith, K.S. Baker, and D.K. Clark. 1988. “A Semianalytical Radiance Model of Ocean Color.” *Journal of Geophysical Research* 93 (D9): 10909–24.

Gordon, H.R., O.B. Brown, and M.M. Jacobs. 1975. “Computed Relationships between Inherent and Apparent Optical Properties of a Flat, Homogeneous Ocean.” *Applied Optics* 14: 417–27.

Gordon, H.R., and A.Y. Morel. 1983. *Remote Assessment of Ocean Color for Interpretation of Satellite Visible Imagery*. New York: Springer-Verlag.

Gordon, H.R., and M. Wang. 1994. “Retrieval of Water-Leaving Radiance and Aerosol Optical Thickness over the Oceans with SeaWiFS: A Preliminary Algorithm.” *Applied Optics* 33 (3): 443–52.

Govaerts, Y., and M. Clerici. 2004. “MSG-1/SEVIRI Solar Channels Calibration Commissioning Activity Report.” *EUMETSAT Doc. EUM/MSG/TEN/04/2004*.

ISO, I.S.O. 1999. “Water Quality - Determination of Turbidity” ISO 7027.

Kou, L., D. Labrie, and P. Chylek. 1993. “Refractive Indices of Water and Ice in the 0.65µm to 2.5µm Spectral Range.” *Applied Optics* 32: 3531–40.

Loisel, H., and A. Morel. 2001. “Non-Isotropy of the Upward Radiance Field in Typical Coastal (Case 2) Waters.” *International Journal of Remote Sensing* 22 (2): 275–95.

Lutz, H. J. 1999. “Cloud Processing for Meteosat Second Generation.” *EUMETSAT Tech Dep*.

Morel, A., and B. Gentili. 1991. “Diffuse Reflectance of Oceanic Waters: Its Dependence on Sun Angle as Influenced by the Molecular Scattering Contribution.” *Applied Optics* 30 (30): 4427–38.

———. 1993. “Diffuse Reflectance of Oceanic Waters II. Bidirectional Aspects.” *Applied Optics* 32: 6864–79.

———. 1996. “Diffuse Reflectance of Oceanic Waters. III. Implications of Bidirectionality for the Remote Sensing Problem.” *Applied Optics* 35 (24): 4850–62.

Morel, A., and L. Prieur. 1977. “Analysis of Variations in Ocean Color.” *Limnology and Oceanography* 22 (4): 709–22.

Nechad, B., K.G. Ruddick, and G. Neukermans. 2009. “Calibration and Validation of a Generic Multisensor Algorithm for Mapping of Turbidity in Coastal Waters.” In *SPIE European International Symposium on Remote Sensing*. Vol. 7473.

Nechad, B., K. G. Ruddick, and Y. Park. 2010. “Calibration and Validation of a Generic Multisensor Algorithm for Mapping of Total Suspended Matter in Turbid Waters.” *REMOTE SENSING OF ENVIRONMENT* 114 (4): 854–66. doi:10.1016/j.rse.2009.11.022.

Neukermans, G., H. Loisel, X. Mériaux, R. Astoreca, and D. McKee. 2012. “In Situ Variability of Mass Specific Beam Attenuation and Backscattering of Marine Particles with Respect to Particle Size, Density and Composition.” *Limnology and Oceanography* 75 (1): 124–44.

Neukermans, Griet, Kevin Ruddick, Emilien Bernard, Didier Ramon, Bouchra Nechad, and Pierre-Yves Deschamps. 2009. “Mapping Total Suspended Matter from Geostationary Satellites: A Feasibility Study with SEVIRI in the Southern North Sea.” *OPTICS EXPRESS* 17 (16): 14029–52. doi:10.1364/OE.17.014029.

Neukermans, G., K. G. Ruddick, and N. Greenwood. 2012. “Diurnal Variability of Turbidity and Light Attenuation in the Southern North Sea from the SEVIRI Geostationary Sensor.” *REMOTE SENSING OF ENVIRONMENT* 124 (September): 564–80. doi:10.1016/j.rse.2012.06.003.

Park, YJ, and K Ruddick. 2005. “Model of Remote-Sensing Reflectance Including Bidirectional Effects for Case 1 and Case 2 Waters.” *APPLIED OPTICS* 44 (7): 1236–49. doi:10.1364/AO.44.001236.

Ruddick, Kevin, Vera De Cauwer, Young-Je Park, and Gerald Moore. 2006. “Seaborne Measurements of near Infrared Water-Leaving Reflectance: The Similarity Spectrum for Turbid Waters.” *Limnology and Oceanography* 51 (2): 1167–79.

Ruddick, KG, V De Cauwer, YJ Park, and G Moore. 2006. “Seaborne Measurements of near Infrared Water-Leaving Reflectance: The Similarity Spectrum for Turbid Waters.” *LIMNOLOGY AND OCEANOGRAPHY* 51 (2): 1167–79.

Ruddick, KG, F Ovidio, and M Rijkeboer. 2000. “Atmospheric Correction of SeaWiFS Imagery for Turbid Coastal and Inland Waters.” *APPLIED OPTICS* 39 (6): 897–912. doi:10.1364/AO.39.000897.

Shi, W., and M. Wang. 2009. “An Assessment of the Black Ocean Pixel Assumption for MODIS SWIR Bands.” *Remote Sensing of Environment* 113: 1587–97.

Steinmetz, F., P.-Y. Deschamps, and D. Ramon. 2011. “Atmospheric Correction in Presence of Sun Glint: Application to MERIS.” *Optics Express* 19 (10): 9783–9800.

Vanhellemont, Q., G. Neukermans, and K. Ruddick. 2013. “High Frequency Measurement of Suspended Sediments and Coccolithophores in European and African Coastal Waters from the Geostationary SEVIRI Sensor.” In .

Vanhellemont, Q., and K. Ruddick. 2015. “Advantages of High Quality SWIR Bands for Ocean Colour Processing: Examples from Landsat-8.” *Remote Sens. Environ.*

Vanhellemont, Quinten, Griet Neukermans, and Kevin Ruddick. 2014. “Synergy between Polar-Orbiting and Geostationary Sensors: Remote Sensing of the Ocean at High Spatial and High Temporal Resolution.” *REMOTE SENSING OF ENVIRONMENT* 146 (SI): 49–62. doi:10.1016/j.rse.2013.03.035.

Vanhellemont Q. & Ruddick K. Pan-sharpening to improve spatial resolution of optical remote sensing with examples from Landsat-8 (30m/15m) (2015) Poster presented at the International Ocean Color Science meeting, held 15 - 18 June 2015, San Francisco.

Viollier, M., D. Tanré, and P.Y. Deschamps. 1980. “An Algorithm for Remote Sensing of Water Color from Space.” *Boundary Layer Meteorology*, no. 18: 247–67.

1 Scope of this Document

This report is a third and final update of the Advanced Theoretical Basis Document (ATBD) of the EUMETSAT-funded SEVIRI-WT project and corresponds to deliverable D3.1 from Task C of the Statement of Work (SOW) EUM/TSS/SOW/14/762098. The present document gives quite a complete description of the algorithms proposed for pixel identification and all aspects of atmospheric correction as well as standardisation of reflectance products for different SEVIRI sensors ("band-shifting", temporal averaging, neglection of bidirectional effects) and derivation of higher resolution products from the High Resolution Visible (HRV) band and the L2W algorithms for turbidity and SPM.

The SEVIRI-WT project will implement and validate a pre-operational processor to generate historical and near real-time Meteosat Second generation (MSG) Spinning Enhanced Visible and Infrared Imager (SEVIRI) ocean colour products, such as water turbidity and light attenuation every 15 minutes for Europe, Africa and the Atlantic Ocean as well as some of the Middle East and Brazil. This document describes in detail the algorithms to be used for generating these products, including both the atmospheric correction and the level 2 water (L2W) products.

The intended readership of this report is:

- The SEVIRI-WT project team, mainly to provide the essential algorithm documentation for development of the processor.
- EUMETSAT managers/engineers to follow the project and comment as appropriate.
- Future users of the SEVIRI-WT output products requiring traceability of processing steps.

2 Change Log

Version	Date	Short Description	Author
0.1	2015.09.15	Template (table of contents)	Kevin Ruddick (RBINS)
0.3		Overall structure including standardisation of reflectance products (band-shifting) and high resolution products	Kevin Ruddick (RBINS)
0.9		Incorporation of atmospheric correction algorithm details and results	Quinten Vanhellemont (RBINS)
0.10		Incorporation of L2W/S algorithms	Bouchra Nechad (RBINS)
1.0		Draft v1 for discussion at PKP4	
1.1	2015.12.23	Completion of L2W/S algorithms (clarification of T algorithm, addition of SPM and bbp640 algorithms) and Addition of L2W/K algorithms	Kevin Ruddick (RBINS)
1.2	2016.01.20	Coefficients AT and CT added for HRV	Kevin Ruddick

		sharpening. See Tables 4 and 5. Also minor update of figure 15 and modification of A785 coefficient from 1810.66*π to 1842.1*π using a few new in situ data points.	(RBINS)
1.3	2016.02.16	Final edits, clean up and formatting (e.g. equation numbering).	Kevin Ruddick (RBINS)
1.4	2016.03.02	Confusion over use of Rrs and Rhow removed in section 8.1 (Turbidity) following comments in Validation section of Final Review Meeting. New terminology for coefficients Ars and Crs introduced to clarify that these are coefficients for the Rrs variant of the algorithm. Changes highlighted in yellow in p44-48.	Kevin Ruddick (RBINS)
1.5	2016.03.02	Highlighting of v1.4 removed.	Kevin Ruddick (RBINS)

3 Introduction

In prior research, (G. Neukermans et al. 2009) established the feasibility of using the geostationary SEVIRI sensor for mapping of Suspended Particulate Matter (SPM) in the turbid waters of the North Sea. In a follow-up paper, (G. Neukermans, Ruddick, and Greenwood 2012) demonstrated a similar capability for mapping of turbidity and light attenuation in these waters. The methodology was further extended to other regions by (Q. Vanhellemont, Neukermans, and Ruddick 2013) and improved, for example using multitemporal averaging to reduce noise, by (Q. Vanhellemont, Neukermans, and Ruddick 2014).

These research activities are being matured into a prototype operational processor for the full SEVIRI disk in the present contract with generation of the products proposed in the Product Document Definition (PDD, D1.2), as motivated by the User Requirements Document (URD, D1.1).

In the present document the algorithms developed in previous research activities are being further improved and analysed and, where necessary, supplemented with new algorithms. The operational, full disk context, in particular, adds new requirements, for example, as regards aerosol correction in regions with a wide range of clear/turbid waters and cloud cover. Certain products, requested by users have not previously been covered by research activities and are addressed for the first time here. An overview of prior and new (this contract) algorithm development work in given in Table 1.

Product	**Prior SEVIRI research**	**Refinements in this contract**
Remote sensing reflectance spectrum at water level	N2009, N2012, V2013, V2014	Full disk aerosol subregion division Non-linear water reflectance model NIR1.6 band black pixel option Adaptation of all LUT to different MSG platforms Refinement of HRV approach Standardisation of wavelength (“band shifting”) Output of VIS0.8 reflectances
Suspended Particulate Matter	N2009	Calibration and validation revisited Nominal wavelength approach Estimated from T using HIGHROC SPM/T dataset
Turbidity	N2012	Calibration and validation revisited Nominal wavelength approach
Particulate backscatter at 640nm	-	Estimated from T using data of (Neukermans et al, 2012)
Secchi Depth	-	Estimated using (Devlin, 2008)
Diffuse attenuation coefficient of PAR	N2012	Validation revisited
Euphotic depth	-	Direct from PAR attenuation
Coccolithophore bloom	(V2013)	Requires further research using multitemporal full disk data from processor
Extreme High Biomass algal bloom	-	Requires further research using multitemporal full disk data from processor

Extreme cyanobacteria bloom/surface scum	-	Requires further research using multitemporal full disk data from processor
Pixel identification (water/cloud/land) and other geophysical	N2009, V2013	Improved cloud (non-water) mask

Table 1 A list of products to be generated (according to the Product Definition Document, D2.1), key references for algorithms suggested previously for SEVIRI and the main progress main in the present contract. N2009, N2012, V2013 and V2014 refer respectively to (G. Neukermans et al. 2009; G. Neukermans, Ruddick, and Greenwood 2012; Q. Vanhellemont, Neukermans, and Ruddick 2013; Q. Vanhellemont, Neukermans, and Ruddick 2014). More information on the products can be found in the PDD.

4 Pixel Identification

An overview of the atmospheric correction and pixel identification data flow is given in Figure 1. In that figure, pixel identification is implemented and performed after Rayleigh correction but before the aerosol correction. For the current document pixel identification is presented in a separate chapter.

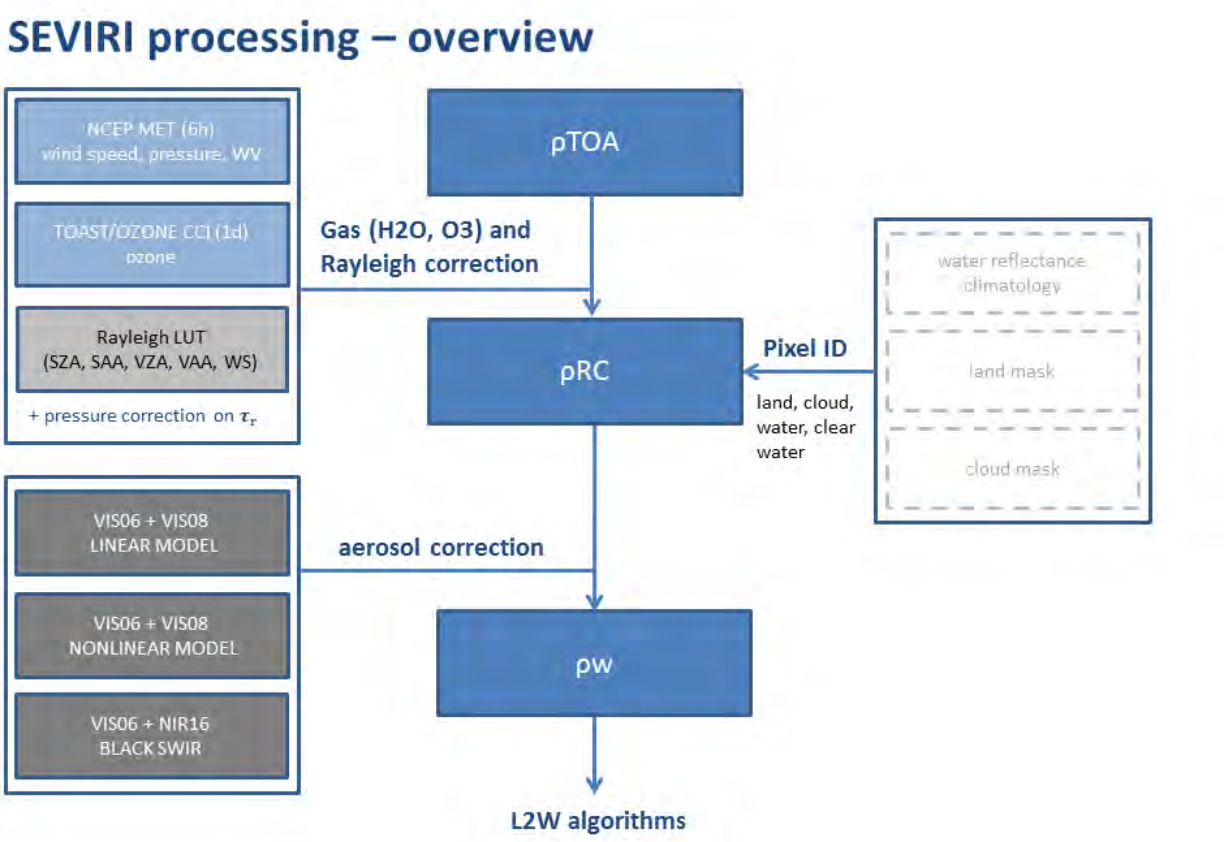

Figure 1 General overview of the processor, showing Pixel Identification, Rayleigh and Gas correction, and the aerosol correction, further detailed in Figure 2.

4.1 Algorithm description

Although not mentioned explicitly in the SOW, the identification of pixels that are not fully occupied by water is an important step of processing, generally handled before the atmospheric correction. For example, pixels may contain partially or fully land rather than water, may contain clouds (the reason MSG was made!) or may be significantly affected by sunglint. A further distinction of regions that generally contain clear water, as opposed to turbid water, is also useful for the aerosol component of the atmospheric correction – see later section 5. The approach adopted for pixel identification in the SEVIRI-WT processor cannot rely solely on existing pixel identification flags, such as the cloud mask, developed for standard EUMETSAT processing because these have been found to be imperfect in prior work (G. Neukermans et al. 2009; G. Neukermans, Ruddick, and Greenwood 2012; Q. Vanhellemont, Neukermans, and Ruddick 2013; Q. Vanhellemont, Neukermans, and Ruddick 2014). This section describes the approach that is recommended for the SEVIRI-WT processor.

Pixel identification into five different classes is proposed:

1) **Land** pixels are determined from a static land mask, provided by HYGEOS.
2) **Cloud** identification can be performed using the standard EUMETSAT cloud mask MSGCLMK based on (Lutz 1999) combined with a 2.15% threshold on reflectance in the NIR1.6 channel. The implementation of both approaches is recommended for the SEVIRI-WT processor, with the NIR1.6 threshold considered at present to be the preferred (default) approach. A similar approach was used in Landsat-8 processing by (Q. Vanhellemont and Ruddick 2015), where a threshold on Rayleigh-corrected reflectance at the 1.6µm band gave effective identification of all non-water pixels[1]. Water pixels (with additional aerosol reflectance) have low NIR1.6 reflectance (hereafter termed "SWIR" [2]), while land, clouds and sunglint all have high SWIR reflectance. For the SEVIRI-WT processor it is thought that a threshold on the NIR1.6 channel will be the best test for identifying non-water pixels and will avoid some flagging of turbid water pixels by the current MSGCLMK mask. It is probably sufficient to apply such a test to top of atmosphere data because the Rayleigh contribution at this band is very low. However, the NIR1.6 threshold test could easily be applied to Rayleigh-corrected data, either using the Rayleigh correction of the full atmosphere correction (which otherwise comes after pixel identification) or using a simplified analytical Rayleigh correction.
3) **Sun glint** pixels are computed using a formulation from HYGEOS using as input the viewing and sun geometry and NCEP derived wind speed.
4) **Water** pixels are those not classified in the classes above, and will be further processed.
5) **Clear water** (low turbidity) pixels are a subset of (4) and are required for the aerosol correction, and are in first instance derived from a MODIS Aqua climatology (http://oceancolor.gsfc.nasa.gov/) for each month using a threshold of 1.2E-4 sr^{-1} on Rrs645, similar to the approach of (G. Neukermans, Ruddick, and Greenwood 2012). These static maps can be later updated using monthly aggregated ρ_w^6 outputs of the SEVIRI-WT processor itself. For this ATBD v1 a similar threshold on SEVIRI Rrs640 is suggested although this threshold may be adapted later to better correspond to the detection limit for water reflectance, which may evolve as processing algorithms improve.

4.2 Algorithm validation

Validation of the pixel identification algorithm will be possible only at a later stage, after the processor has been developed. Testing of the elements of pixel identification is essential and will lead to a clearer understanding of the optimal combination of tests in the full disk context, including for high zenith angle situations.

4.3 Uncertainties

Pixel identification flags will not have uncertainty estimates.

---

[1] Poor performance of the non-water pixel identification was found for Landsat-8 only for some cloud shadows over land which have, like water, low SWIR reflectance. In the SEVIRI context, because of the much larger pixels, cloud shadows will not be a significant problem.

[2] For the ocean colour community, the NIR1.6 (1.6µm) band would generally be considered to be Short Wave Infra Red (SWIR) rather than Near Infrared (NIR), which is often deemed to cover 700-1000nm. Similarly the VIS0.8 band (0.8µm) would generally be considered to be NIR. The term "SWIR" is used in this ATBD for the NIR1.6 for compatibility with other ocean colour publications.

4.4 Quality flagging

The pixel identification flags do not themselves have quality flags attached since they are part of the quality flagging of the processor geophysical outputs.

4.5 Adaptation to different SEVIRI sensors

The different spectral response functions of the different SEVIRI sensors are not expected to make a significant difference to the thresholds used for pixel identification, e.g. as regards the NIR1.6 threshold test. The processor can easily be implemented with the possibility of using a platform-specific threshold, although it is likely that a single value will actually be used for all MSG platforms.

4.6 Algorithm limitations and recommendations for future improvements

Performance of the NIR1.6 threshold test (for top of atmosphere or Rayleigh-corrected data) remains to be tested in a full disk context.

Use of the MSGCLMK cloud mask also needs to be carefully evaluated during the Product Validation Task.

On the basis of prior work, it is expected that the proposed tests will function well although some adaptation of thresholds made be necessary to cover all cases encountered in the full disk.

5 Atmospheric Correction

The atmospheric correction, and in particular the aerosol correction, is the most difficult and critical algorithm for SEVIRI-WT processing. The atmospheric correction is decomposed into a number of steps, which are described here, based largely on prior work of (G. Neukermans et al. 2009; G. Neukermans, Ruddick, and Greenwood 2012; Q. Vanhellemont, Neukermans, and Ruddick 2013; Q. Vanhellemont, Neukermans, and Ruddick 2014). Significant new work regarding the turbid water component of the atmospheric correction and possible use of the NIR1.6 band are described in the present document. Improvements have also been made to the LUT, using a spherical shell model for the Rayleigh correction, and using an improved method for estimating aerosol diffuse transmittance from the retrieved aerosol type and reflectance. The method for identifying clear water pixels and spatially extrapolating aerosol type information is also generalised here for the full disk context.

Details of the components of the atmospheric correction are illustrated in Figure 2.

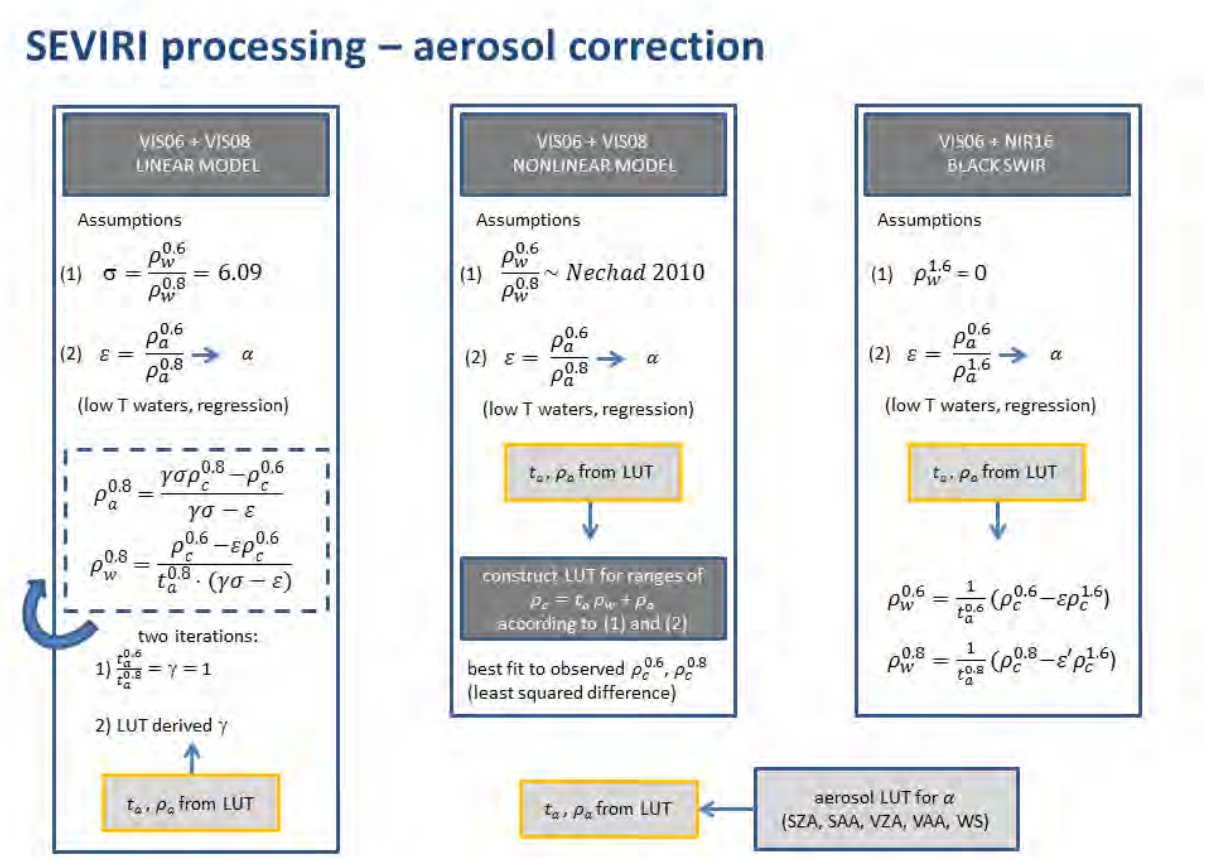

Figure 2 Overview of the three different aerosol correction schemes, (1) linear water reflectance model, (2) nonlinear water reflectance model, the default option, and (3) assuming black SWIR over water.

5.1 Algorithm description

The atmospheric correction algorithm developed by (G. Neukermans et al. 2009) assumes that the signal recorded by the SEVIRI sensor at the top of atmosphere (TOA) is the sum of marine and atmospheric contributions. The TOA signal is thus simplified to:

$$\rho_{TOA} = \rho_r + \rho_a + t \cdot \rho_w , \qquad 1$$

where ρ_r is the Rayleigh reflectance, ρ_a the aerosol reflectance (including multiple aerosol-aerosol, aerosol-Rayleigh and aerosol-surface effects), and t the two-way sun-sea, sea-sensor diffuse atmospheric transmittance. The parameter of interest is the water-leaving radiance reflectance, or water reflectance (ρ_w), and thus the other parts contributing to the ρ_{TOA} have to be accurately estimated and removed.

Surface effects, other than the Fresnel reflectance of skylight (considered in the Rayleigh and aerosol components), are not explicitly corrected for in the algorithm, as (1) the contribution of whitecaps to a SEVIRI pixel has not been studied, but whitecaps generally have a similar spectral shape as aerosols, and will thus be largely corrected for in the aerosol correction, and (2) sun glint correction requires specialised processing to perform well, e.g. (Steinmetz, Deschamps, and Ramon 2011). Sun glint could be safely ignored by (G. Neukermans et al. 2009) as their study area lies outside the specular reflection geometry for SEVIRI. For a geostationary sensor the sunglint is always located in the tropics. In the case of the full disk, the sun glint area will be computed and simply masked (section 4.1).

5.1.1 Absorbing gas and Rayleigh correction

The scattering by air molecules, or Rayleigh scattering, depends on the air mass between the sun, the target and the sensor. Rayleigh reflectance can be computed for a known viewing and sun geometry, wind speed, and corrected for atmospheric pressure.

Ancillary data files used in the processing are 6-hourly, 1° global NCEP MET files for atmospheric pressure, wind speed and water vapour concentration, linearly interpolated to the image acquisition time, and daily files for the ozone concentration (from TOAST or ESA Ozone CCI). Ancillary data fields are resampled to the SEVIRI L1.5 grid and spatially smoothed to remove sharp boundaries.

The ρ_{TOA} is corrected for water vapour and ozone transmittances (t_{wv} and t_{oz}), derived from concentrations in the MET and ozone ancillary data, giving the gas corrected reflectance, ρ_{gc}:

$$\rho_{gc} = \frac{\rho_{TOA}}{t_{oz} \cdot t_{wv}} \qquad 2$$

In the previous processing chains, the Rayleigh reflectance was estimated using an analytical formula (Viollier, Tanré, and Deschamps 1980) or a more accurate pre-generated LUT using 6SV simulations (Griet Neukermans et al. 2009; G. Neukermans, Ruddick, and Greenwood 2012; Q. Vanhellemont, Neukermans, and Ruddick 2013). 6SV uses a plane-parallel atmosphere and will overestimate Rayleigh reflectance at high viewing or sun zenith angles.

For the full disk processor the LUT will be updated using a more accurate spherical shell modelling appropriate for these high angles generated using the GPU enabled Monte Carlo simulation tool, SMART-G.

The LUT contains Rayleigh reflectance as function of view and sun zenith angles (θ_v and θ_s), the relative azimuth angle between the two (ϕ) and wind speed (w) for nominal surface pressure (P0 = 1013.25 hPa). These angles and wind speeds are known for each pixel in the SEVIRI disk, and Rayleigh reflectance at nominal pressure, ρ_r^{P0} is computed from the LUT. Diffuse Rayleigh transmittances ($t_r = t_{rd} \cdot t_{ru}$) are computed analytically:

$$t_r\ (\theta) = \exp\left(-\frac{\tau_r^P}{2\cos\theta}\right) \qquad 3$$

where θ is the sun zenith or viewing zenith angle to give the transmittances respectively in the down and upward directions, τ_r^P is the Rayleigh optical thickness adjusted for observed pressure:

$$\tau_r^P = \tau_r^{P0} \frac{P}{P0} \qquad 4$$

with τ_r^{P0} the Rayleigh optical thickness for a standard atmosphere, P the observed atmospheric pressure (from NCEP data) and P0 the standard atmospheric pressure. The ρ_{gc} is thus corrected for Rayleigh diffuse transmittance and Rayleigh reflectance, giving Rayleigh and gas-corrected reflectances, ρ_c in each band:

$$\rho_c = \frac{\rho_{gc}}{t_{ru} \cdot t_{rd}} - \rho_r^{P0} \qquad 5$$

5.1.2 Aerosol correction

Over turbid waters, the VIS0.6 and VIS0.8 channels are affected both by aerosols and by water and the simple “black NIR pixel” aerosol correction of (Gordon and Wang 1994) cannot be used. In fact, since SEVIRI has no other channels in the visible a black pixel aerosol approach would mean zero output from the SEVIRI-WT processor everywhere. Separation of aerosol and water reflectances fundamentally requires two assumptions, one regarding the spectral variation of aerosol the other regarding the water reflectances.

Thus,

- Spatial homogeneity of aerosol type is assumed at least over short length scales (KG Ruddick, Ovidio, and Rijkeboer 2000), enabling spatial extrapolation of aerosol type obtained using a black pixel assumption for clear waters to neighbouring turbid waters.
- As regards the water reflectances three possible assumptions have been identified:
    - A linear model relating reflectance at the VIS0.6 and VIS0.8 bands was used by (G. Neukermans et al. 2009).
    - An improved non-linear water reflectance model is suggested in the present document.
    - Instead of the VIS0.8 band the NIR1.6 band, where water reflectance is always zero, can be used.

These approaches and discussion of the pros and cons of the alternative assumptions for water reflectance are discussed in the following subsections.

5.1.2.1 Assumption on the aerosol type

It is assumed that the spectral dependency of aerosol reflectance (termed 'aerosol type', although this term is used loosely in the present multiple-scattering context) does not vary over relatively short spatial scales, and can be determined over clear (low turbidity) water pixels with negligible water reflectance. In these pixels, the aerosol reflectance is equal to the Rayleigh and gas corrected reflectance, and the ratio between the aerosol reflectances in VIS0.6 and VIS0.8, $\varepsilon^{0.6,0.8}$, or the angstrom exponent of aerosol reflectance, α, can be derived:

$$\varepsilon^{0.6,0.8} = \frac{\rho_a^{0.6}}{\rho_a^{0.8}} = \frac{\rho_c^{0.6}}{\rho_c^{0.8}} \quad (6)$$

$$\alpha = -\frac{log\left(\rho_a^{0.6}/\rho_a^{0.8}\right)}{log\left(\lambda^{0.6}/\lambda^{0.8}\right)} = -\frac{log\left(\varepsilon^{0.6,0.8}\right)}{log\left(\lambda^{0.6}/\lambda^{0.8}\right)} \quad (7)$$

The aerosol ε can be estimated from the mean ratio of $\rho_a^{0.6}$ and $\rho_a^{0.8}$ over clear water pixels (G. Neukermans et al. 2009) or, alternatively, from the slope of an iterative robust linear regression between $\rho_a^{0.6}$ and $\rho_a^{0.8}$ over clear water pixels (G. Neukermans, Ruddick, and Greenwood 2012). Depending on the method used, the uncertainty caused by the uncertainty on aerosol type estimation ($\Delta\varepsilon$) will be computed using the standard deviation of the ratio of $\rho_a^{0.6}$ and $\rho_a^{0.8}$ or using the standard error on the robust linear regression slope estimate. As a third alternative a median ratio of $\rho_a^{0.6}$ and $\rho_a^{0.8}$ over clear water pixels can be used and is more robust to outliers (as used for Landsat-8 processing by (Q. Vanhellemont and Ruddick 2015)), and assuming a normal distribution, $\Delta\varepsilon$ can be estimated from the interquartile range: (p75-p25)/(2x0.67), where p25 and p75 are the 25th and 75th percentiles, and 0.67 the absolute value of the standard score of p25 and p75 in the normal distribution.

For the SEVIRI-WT processor the full disk will be split into subregions, as explained in detail in section 5.1.2.6 and illustrated in Figure 9, with a single aerosol $\varepsilon^{0.6,0.8}$ estimated for each subregion and a methodology for weighting the values from neighbouring subregions to give the $\varepsilon^{0.6,0.8}$ to be used for any specific pixel.

For the SEVIRI-WT processor, the iterative robust linear regression is recommended as default, and the slope (ε) with standard error ($\Delta\varepsilon$) and offset should be stored for each subregion. The linear regression method of (G. Neukermans, Ruddick, and Greenwood 2012) allowed effectively for a per-image vicarious calibration using the offset of this regression line. It is not clear whether this is still an optimal approach in the full disk context with potentially different offsets in different subregions. The offset will therefore not be applied in the first version of the processor but will be analysed during the Product Validation task to provide information on the quality of the Rayleigh correction and possible vicarious calibration.

5.1.2.2 Assumption on the water reflectance

The three possible assumptions for the water reflectance are given here:

1) The water reflectance in the VIS0.6 and VIS0.8 follows a known relationship.(G. Neukermans et al. 2009) and (G. Neukermans, Ruddick, and Greenwood 2012) used a linear model, recalibrated by the latter:

$$\boldsymbol{\sigma = \frac{\rho_w^{0.6}}{\rho_w^{0.8}} = 6.02,} \qquad 8$$

with associated uncertainty (standard deviation in 47 reflectance measurements) of $\Delta\sigma$ = 0.16. At moderate turbidities, this model corresponds well to the theory and results from (K. Ruddick et al. 2006), but it is known that for higher turbidities the relationship becomes nonlinear, as seen from simulated data in Figure 4 of (KG Ruddick et al. 2006), from in situ data in Figure 5 of (G. Neukermans et al. 2009) and discussed in detail in (Doron et al. 2011).

2) An improved analytical non-linear model is suggested here where the VIS0.6 and VIS0.8 are inter-related using the turbidity retrieval model of (Nechad, Ruddick, and Park 2010). This approach has the interested feature of ensuring that L2W/S products, described later in section 8, can be derived from either Rrs640 or Rrs785 in an entirely consistent way. According to this analytical model, which is described further in Annex A:

$$\rho_w^{0.6} = \rho_w^{0.8} \frac{A_T^{0.6}}{A_T^{0.6} + \rho_w^{0.8}\left(A_T^{0.8}/C^{0.6} - A_T^{0.6}/C^{0.8}\right)} \qquad 9$$

where the coefficients are obtained from calibration of the Turbidity retrieval algorithm, either specifically for each SEVIRI sensor or, via the band-shifting approach described later in section 6.1, for the nominal Rrs640 and Rrs785 wavelengths.

3) A third alternative is to use the NIR1.6 band instead of the VIS0.8 band. In the NIR1.6 channel, the water absorption is so high (Kou, Labrie, and Chylek 1993) that even in the most turbid waters the water-leaving radiance reflectance can be assumed zero (Shi and Wang 2009):

$$\rho_w^{1.6} = 0 \qquad 10$$

This means that an estimate of aerosol reflectance can be directly made in the NIR1.6 channel, and a model for the water reflectance is not necessary:

$$\rho_a^{1.6} = \rho_c^{1.6} \qquad 11$$

Using this channel the angstrom exponent of the aerosol reflectance is determined, as for the VIS0.8/VIS0.6 approach, over low turbidity pixels from the ratio of Rayleigh and gas corrected reflectances:

$$\boldsymbol{\varepsilon^{0.6,1.6} = \frac{\rho_a^{0.6}}{\rho_a^{1.6}} = \frac{\rho_c^{0.6}}{\rho_c^{1.6}}} \qquad 12$$

$$\boldsymbol{\alpha = -\frac{log\left(\rho_a^{0.6}/\rho_a^{1.6}\right)}{log\left(\lambda^{0.6}/\lambda^{1.6}\right)} = -\frac{log\left(\varepsilon^{0.6,1.6}\right)}{log\left(\lambda^{0.6}/\lambda^{1.6}\right)}} \qquad 13$$

It should be noted that due to the low signal in the SWIR over water, the low SNR of the NIR1.6 channel and the digitisation in the L1.5 files, the uncertainty on the aerosol estimation will be larger, and the L2 products will be noisier when this band is used in the atmospheric correction. A large advantage is that no water reflectance model needs to be assumed, as there is a direct estimation of the aerosol reflectance, and the water reflectances in VIS0.6 and VIS0.8 can be independently calculated. Some noise reduction can be achieved using temporal averaging of the output L2 products – see section 6.2.

The temporal averaging could potentially be carried out before the aerosol correction at top of atmosphere or after Rayleigh and gas corrections, but such an approach is more complicated

computationally and may suffer from the fast temporal variability of aerosols (and of both the Rayleigh and aerosol reflectances for low sun condition). It is proposed here not to perform temporal averaging until after L2W product generation.

A further alternative of spatial averaging of the water-flagged top of atmosphere NIR1.6 data might be a more promising method to reduce noise in the approach using NIR1.6 for aerosol correction. Some preliminary tests have been carried out in the present study, but require more work, e.g. to define the optimal spatial kernel for averaging, large enough to reduce noise but small enough to capture most natural spatial variability of aerosols.

For the SEVIRI-WT processor it is recommended to implement all three approaches, although the non-linear VIS0.6/VIS0.8 approach is recommended as the default approach. The VIS0.6/NIR1.6 may give better performance for the most turbid water pixels or may provide validation and/or improvement of the non-linear analytical model used in the VIS0.6/VIS0.8 approach. The linear VIS0.6/VIS0.8 approach has known inaccuracies for high reflectance waters, but should be retained because it is the only approach that has been extensively tested in prior work and because it will provide a useful benchmark for testing of the non-linear VIS0.6/VIS0.8 approach.

5.1.2.3 Aerosol correction look-up tables

Look-up tables for the aerosol correction will be generated for a grid of viewing and sun zenith angles, and relative azimuth angles, and a range of angstrom exponents for the three SEVIRI channels, VIS0.6, VIS0.6 and NIR1.6. The final set of models will depend on the ranges of the aerosol exponents encountered in the SEVIRI full disk. Each aerosol model will have an associated single scattering albedo, scattering phase function and extinction coefficient. This will allow the determination of aerosol optical thickness, τ_a and the aerosol transmittance, t_a based on the observed aerosol reflectance ρ_a and taking account of multiple scattering effects.

5.1.2.4 Retrieval of water reflectance ρ_w

The calculation of water reflectances from Rayleigh-corrected using the aerosol and water assumptions detailed in section 5.1.2.1 and 5.1.2.2 is described in detail here for each of the three possible approaches for the water reflectance model. A comparison of the three methods for the southern North Sea and the Amazon River plume are given at the end of this section.

1) Linear water reflectance model

From Equations 6 and 8, and following the reasoning in (KG Ruddick, Ovidio, and Rijkeboer 2000; G. Neukermans et al. 2009), the aerosol and water reflectances, ρ_a and ρ_w, can then be derived in every pixel for each band:

$$\rho_a^{0.8} = \frac{\gamma\sigma\rho_c^{0.8} - \rho_c^{0.6}}{\gamma\sigma - \varepsilon}, \quad 14$$

$$\rho_a^{0.6} = \varepsilon\rho_a^{0.8}, \quad 15$$

$$\rho_w^{0.8} = \frac{\rho_c^{0.6} - \varepsilon\rho_c^{0.6}}{t_a^{0.8}\cdot(\gamma\sigma - \varepsilon)}, \quad 16$$

$$\rho_w^{0.6} = \sigma\rho_w^{0.8}, \quad 17$$

where γ is the ratio of two-way aerosol diffuse transmittances in both bands:

$$\boldsymbol{\gamma} = \frac{\boldsymbol{t_a^{0.6}}}{\boldsymbol{t_a^{0.8}}}. \quad 18$$

γ is determined iteratively: first this ratio is assumed to be 1 and the aerosol optical thickness, τ_a, is estimated from aerosol reflectance and geometry. In the prototype processor at RBINS, a LUT constructed using a single marine aerosol model is used to estimate the aerosol reflectance at the current view and sun geometry for three τ_a (0.01, 0.5, 1.0), and the observed aerosol reflectance is then used to estimate τ_a by linear interpolation. Using the observed τ_a, a second LUT is then used to retrieve t_a. The second iteration takes the ratio of retrieved aerosol

transmittances, γ, in account, giving final estimates of τ_a and t_a. In the full disk processor, the LUT will be extended taking in account multiple possible aerosol models (based on a range of angstrom exponents), and a fitted model for relating ρ_a to t_a.

2) Nonlinear water reflectance model (default)

The nonlinear water reflectance model does not allow for a simple analytical solution for $\rho_w^{0.6}$ and $\rho_w^{0.8}$ as function of $\rho_c^{0.6}$ and $\rho_c^{0.8}$. Instead it is necessary to adopt either an iterative approach or generate a LUT to invert for all possible combinations of $\rho_c^{0.6}$ and $\rho_c^{0.8}$. This latter approach is outlined here by generating such combinations using the forward model giving $\rho_c^{0.6}$ and $\rho_c^{0.8}$ for all possible o$\rho_w^{0.8}$ and $\rho_a^{0.8}$ inputs.

All possible combinations of $\rho_w^{0.8}$ and $\rho_a^{0.8}$ in the observed $\rho_c^{0.8}$ can be computed:

$$\mathbf{0} \leq \boldsymbol{\rho_w^{0.8}} \leq \boldsymbol{C^{0.8}} \quad (19)$$

$$\mathbf{0} \leq \boldsymbol{\rho_a^{0.8}} \leq \boldsymbol{\rho_c^{0.8}} \quad (20)$$

From Equations (6) and (9), the possible ranges of $\rho_w^{0.6}$ and $\rho_a^{0.6}$ in the observed $\rho_c^{0.6}$ are then known:

$$\mathbf{0} \leq \boldsymbol{\rho_w^{0.6}} \leq \boldsymbol{C^{0.6}} \quad (21)$$

$$\boldsymbol{\rho_a^{0.6}} = \boldsymbol{\varepsilon \rho_a^{0.8}} \quad (22)$$

Given these ranges of ρ_a and the aerosol models used in the aerosol LUT generation a summed water and aerosol reflectance LUT is computed spanning the combination of the ranges in $t_a^{0.6} \cdot \rho_w^{0.6}$, $t_a^{0.8} \cdot \rho_w^{0.8}$ and $\rho_a^{0.6}$, $\rho_a^{0.8}$, with the t_a computed from ρ_a and the coefficients from the aerosol LUT. It is suggested to use a spacing of 5E-4 in reflectances for this LUT, corresponding to approximately the digitization in the L1.5 files for a zenith sun. This gives around 400 bins in the water reflectance range, and 600 bins for $\rho_c^{0.8}$ ranging between 0 and 0.3.

The four best fitting values of $t_a^{0.6} \cdot \rho_w^{0.6} + \rho_a^{0.6}$ and $t_a^{0.8} \cdot \rho_w^{0.8} + \rho_a^{0.8}$ (two higher and two lower bounding for the $\rho_c^{0.6}$) are located this table according to the least squared error with the observed $\rho_c^{0.6}$ and $\rho_c^{0.8}$. The four retrieved values for each of the parameters are then linearly weighted to give a single solution for $t_a^{0.6} \cdot \rho_w^{0.6}$, $t_a^{0.8} \cdot \rho_w^{0.8}$, $\rho_a^{0.6}$, and $\rho_a^{0.8}$.

3) NIR1.6 alternative

As the NIR1.6 channel can be assumed to be black over all water pixels, the aerosol reflectance is equal to the Rayleigh and gas corrected reflectance:

$$\rho_a^{1.6} = \rho_c^{1.6} \quad (23)$$

Assuming a spatially fixed aerosol type, $\varepsilon^{0.6,1.6}$, derived from low turbidity pixels, the $\rho_a^{0.6}$ and $\rho_a^{0.8}$ can be derived:

$$\rho_a^{0.6} = \varepsilon^{0.6,1.6} \cdot \rho_c^{1.6}, \quad (24)$$

$$\rho_a^{0.8} = \varepsilon^{0.8,1.6} \cdot \rho_c^{1.6}, \quad (25)$$

where $\varepsilon^{0.8,1.6}$, is computed from the aerosol LUT best fitting to the observed $\varepsilon^{0.6,1.6}$. The water reflectances are then simply given by:

$$\rho_w^{0.6} = \frac{\rho_c^{0.6} - \rho_a^{0.6}}{t_a^{0.6}}, \quad (26)$$

$$\rho_w^{0.8} = \frac{\rho_c^{0.8} - \rho_a^{0.8}}{t_a^{0.8}}, \quad (27)$$

where the diffuse aerosol transmittances are computed from the ρ_a and coefficients in the aerosol LUT.

5.1.2.5 Tests of the three approaches for modelling water reflectance in the aerosol correction

Since the nonlinear water reflectance model and the NIR1.6 black pixel methods have been newly developed in this study, some results showing their respective performance are included here.

In **Figure 3** results are shown for water and aerosol reflectances retrieved using the three different approaches for treatment of the turbid water reflectance described in section 5.1.2.2. These results show that the non-linear water reflectance model gives much better (but not perfect) separation between water and aerosol reflectances than the linear model since turbid water residuals in the aerosol reflectance map are reduced. For the NIR1.6-based approach these turbid water residuals are no longer visible in the aerosol maps indicating good separation, however there is generally more noise for the water reflectance maps.

In Figure 4 a scatterplot analysis of the same results shows that the linear and non-linear indeed have the imposed relationship between the two water reflectances. Interesting the NIR1.6-based approach which does not impose any such relationship returns a similar relationship to the non-linear water reflectance model, giving independent support for the latter, although some variability can also be observed. This variability may be from noise in the SEVIRI imagery, from ignored spatial variability of aerosol type impacting the water reflectance retrievals and/or from natural variability of the relationship between the two water reflectances.

In Figure 5 the same results are further analysed by scatterplots comparing the water reflectances obtained with the 3 different approaches. The systematic underestimation at high reflectance of the linear model compared to the non-linear and NIR1.6-based approaches indicates the clear limitation of the former approach for the more turbid waters.

In Figure 6, **Figure 7** and Figure 8 a similar analysis is made for SEVIRI imagery of the Amazon plume, where the water is significantly more turbid than in the southern North Sea. Conclusions are quite similar to the conclusions drawn from the North Sea tests, but with an extension of the range of data into extremely turbid waters. The results for the SWIR approach in **Figure 7** are especially interesting for validation of the non-linear water reflectance model.

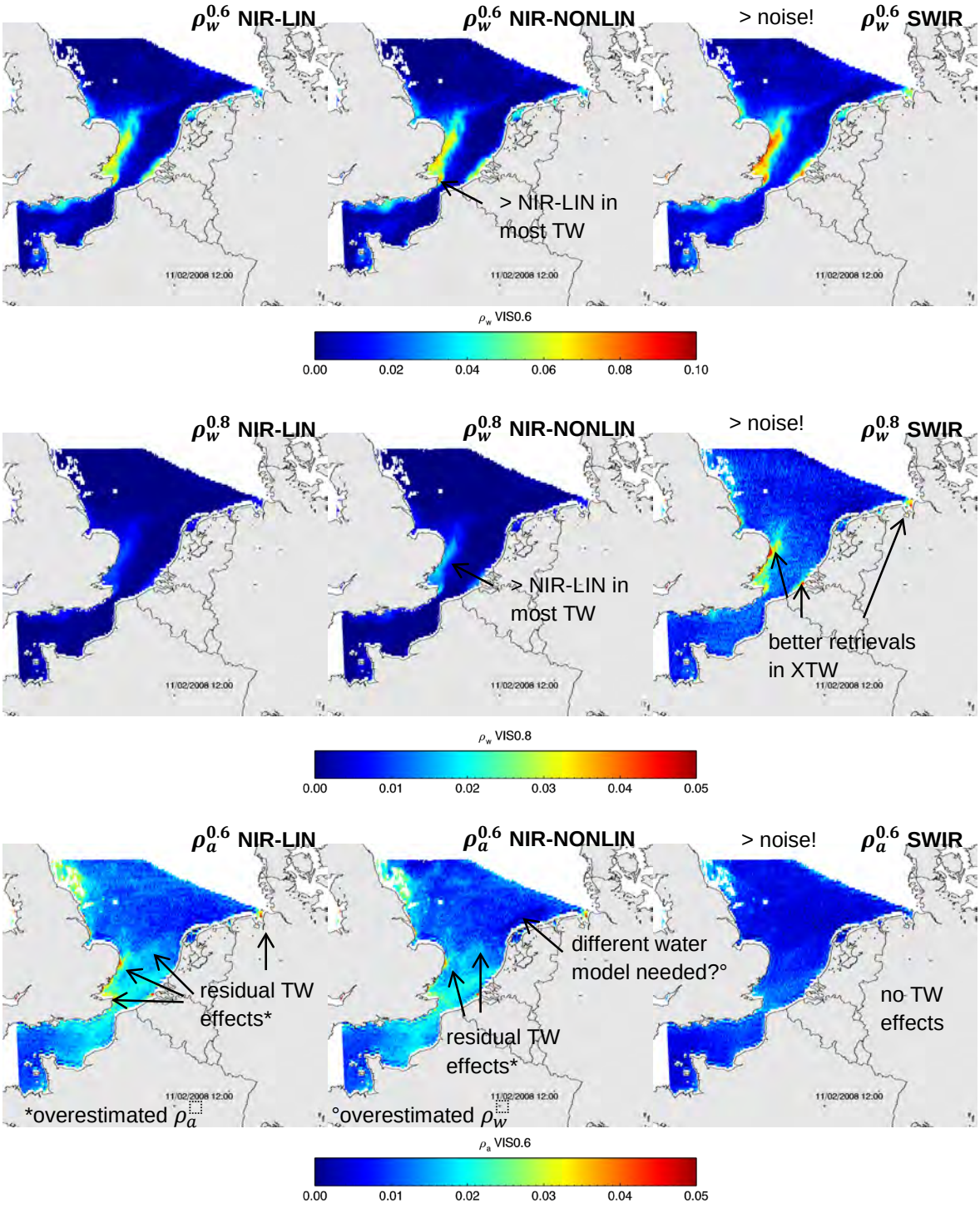

Figure 3 A SEVIRI sub-scene of the southern North Sea on 2008-02-11 at 12:00 UTC, processed with the RBINS prototype processor, using the NIR based aerosol correction, using the linear water model (left), the nonlinear water model (middle) and (right) the SWIR based aerosol correction. The top two rows shows the retrieved water reflectance in the VIS06 and VIS0.8 channels, $\rho_w^{0.6}$ and $\rho_w^{0.8}$ the bottow row shows the aerosol reflectance in the VIS0.6 channel, $\rho_a^{0.6}$. For the SWIR atmospheric correction, $\varepsilon^{0.8,1.6}$ is determined from $\varepsilon^{0.6,1.6}$ using an exponential interpolation.

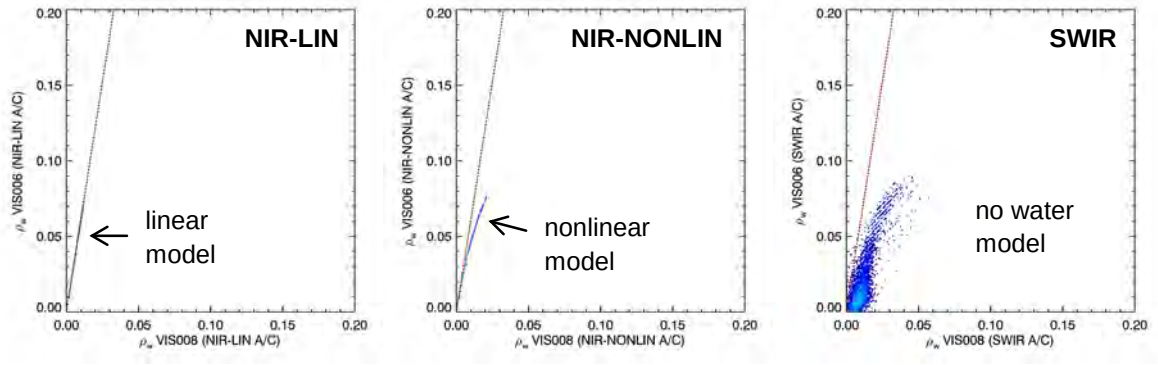

Figure 4 The retrieved relationship between the water reflectances in the VIS0.6 and VIS0.8 channels for the southern North Sea on 2008-02-11 at 12:00 UTC (Figure 3), using the RBINS prototype processor, the NIR based aerosol correction, with linear model (NIR-LIN, left), nonlinear model (NIR-NONLIN, middle), and the SWIR based aerosol correction (SWIR, right). The red dashed line shows the model used by (G. Neukermans et al. 2009). The linear and nonlinear models used in the atmospheric correction can be clearly seen in the left and middle plots, while the SWIR correction shows more spread around the NIR-NONLIN model, caused both by natural variability in the VIS0.6-VIS0.8 relationship of water reflectances and noise in the NIR1.6 channel.

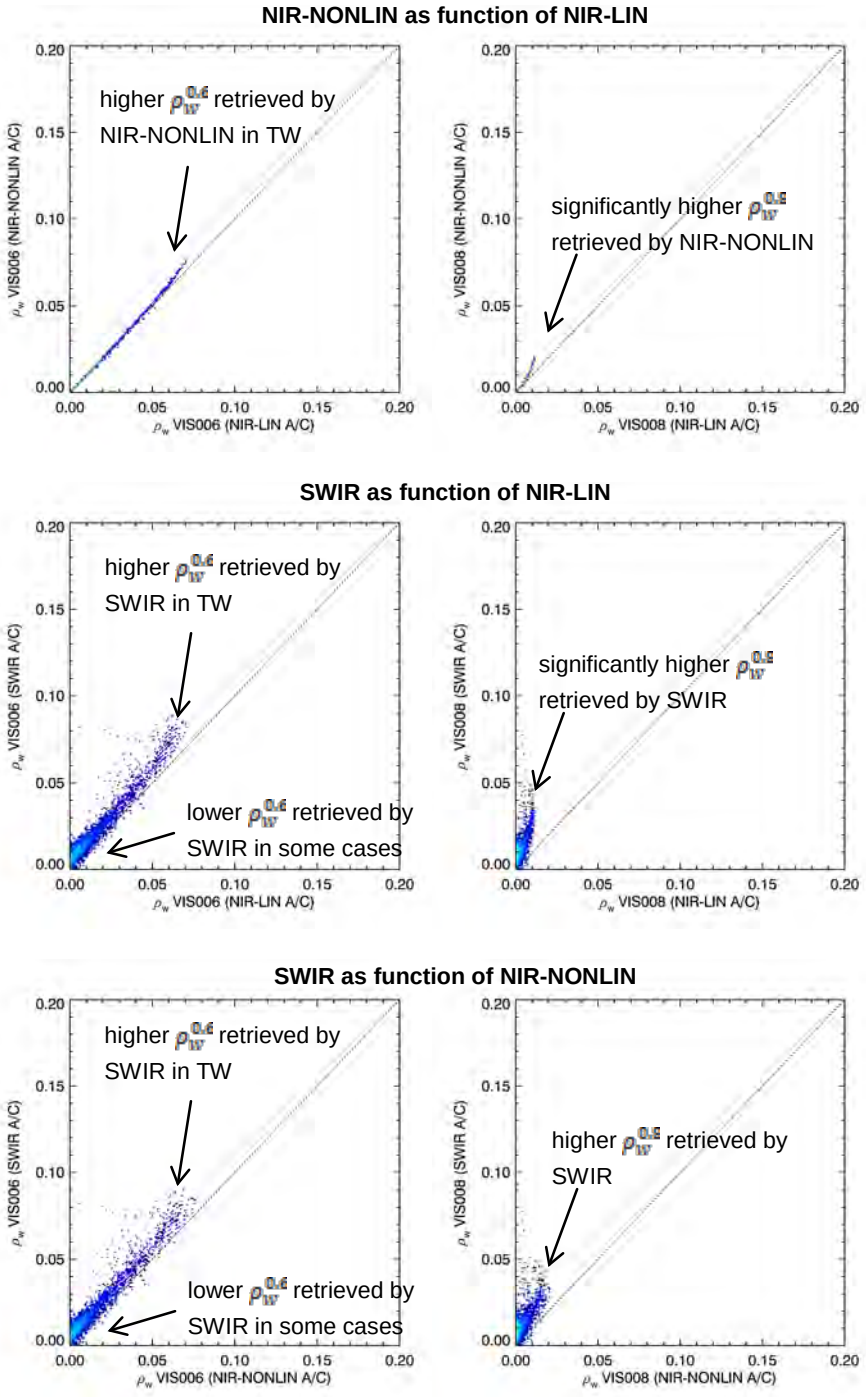

Figure 5 Comparison of the water reflectances in the VIS0.6 (left) and VIS0.8 (right) channels for the southern North Sea on 2008-02-11 at 12:00 UTC (Figure 3) using different aerosol corrections in the RBINS prototype processor. Top row: NIR-NONLIN compared to NIR-LIN, middle row: SWIR compared to NIR-LIN, and bottom row: NIR-NONLIN compared to SWIR. The dashed line shows the 1:1 line.

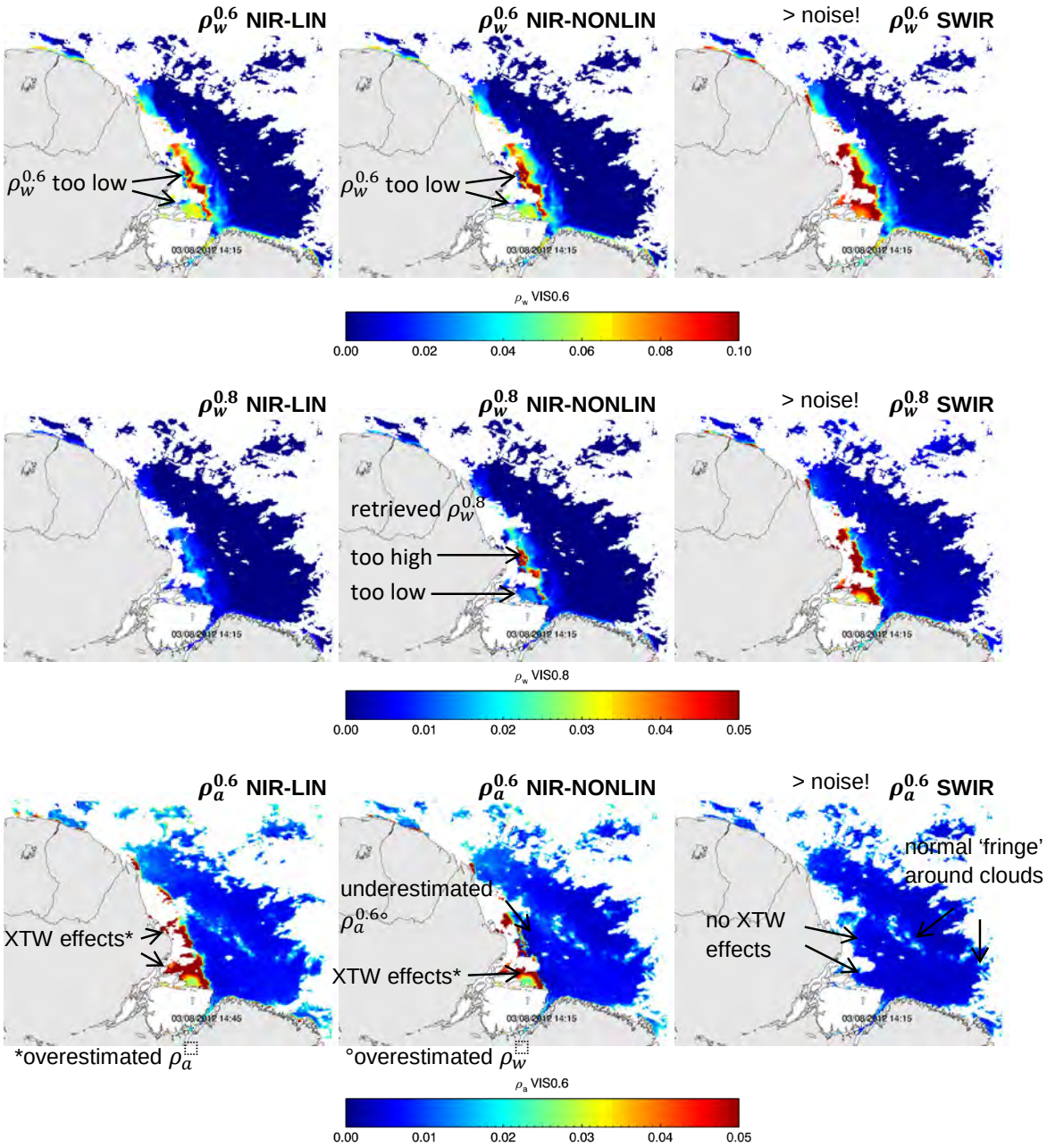

Figure 6 A SEVIRI sub-scene of the Amazon River plume on 2012-08-03 at 14:15 UTC, processed with the RBINS prototype processor using the NIR based aerosol correction, using the linear water model (left), the nonlinear water model (middle) and (right) the SWIR based aerosol correction. The top two rows shows the retrieved water reflectance in the VIS06 and VIS0.8 channels, $\rho_w^{0.6}$ and $\rho_w^{0.8}$ the bottow row shows the aerosol reflectance in the VIS0.6 channel, $\rho_a^{0.6}$. For the SWIR atmospheric correction, $\varepsilon^{0.8,1.6}$ is determined from $\varepsilon^{0.6,1.6}$ using an exponential interpolation.

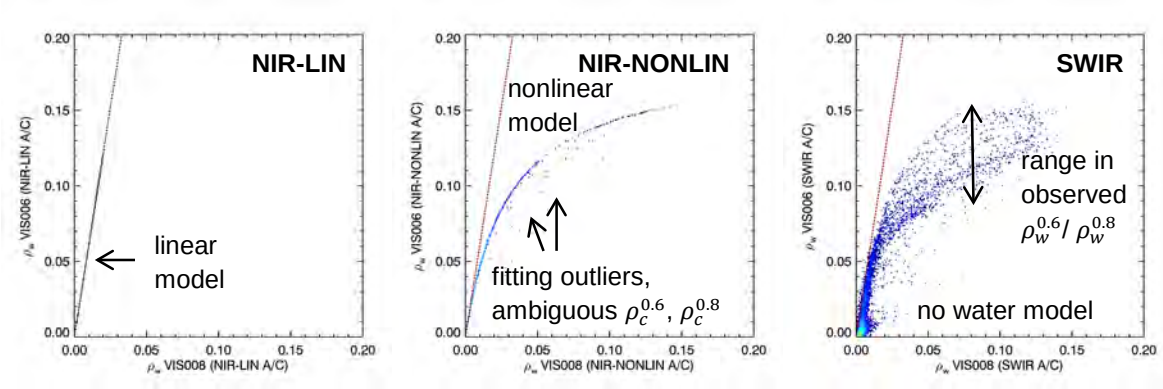

Figure 7 The retrieved relationship between the water reflectances in the VIS0.6 and VIS0.8 channels for the Amazon River plume on 2012-08-03 at 14:15 UTC (Figure 6) using the RBINS prototype processor, the NIR based aerosol correction, with linear model (NIR-LIN, left), nonlinear model (NIR-NONLIN, middle), and the SWIR based aerosol correction (right). The red dashed line shows the model used by (G. Neukermans, Ruddick, and Greenwood 2012). The linear and nonlinear models used in the atmospheric correction can be clearly seen in the left and middle plots, while the SWIR correction shows more spread around the NIR-NONLIN model, caused both by natural variability in the VIS0.6-VIS0.8 relationship of water reflectances and noise in the NIR1.6 channel.

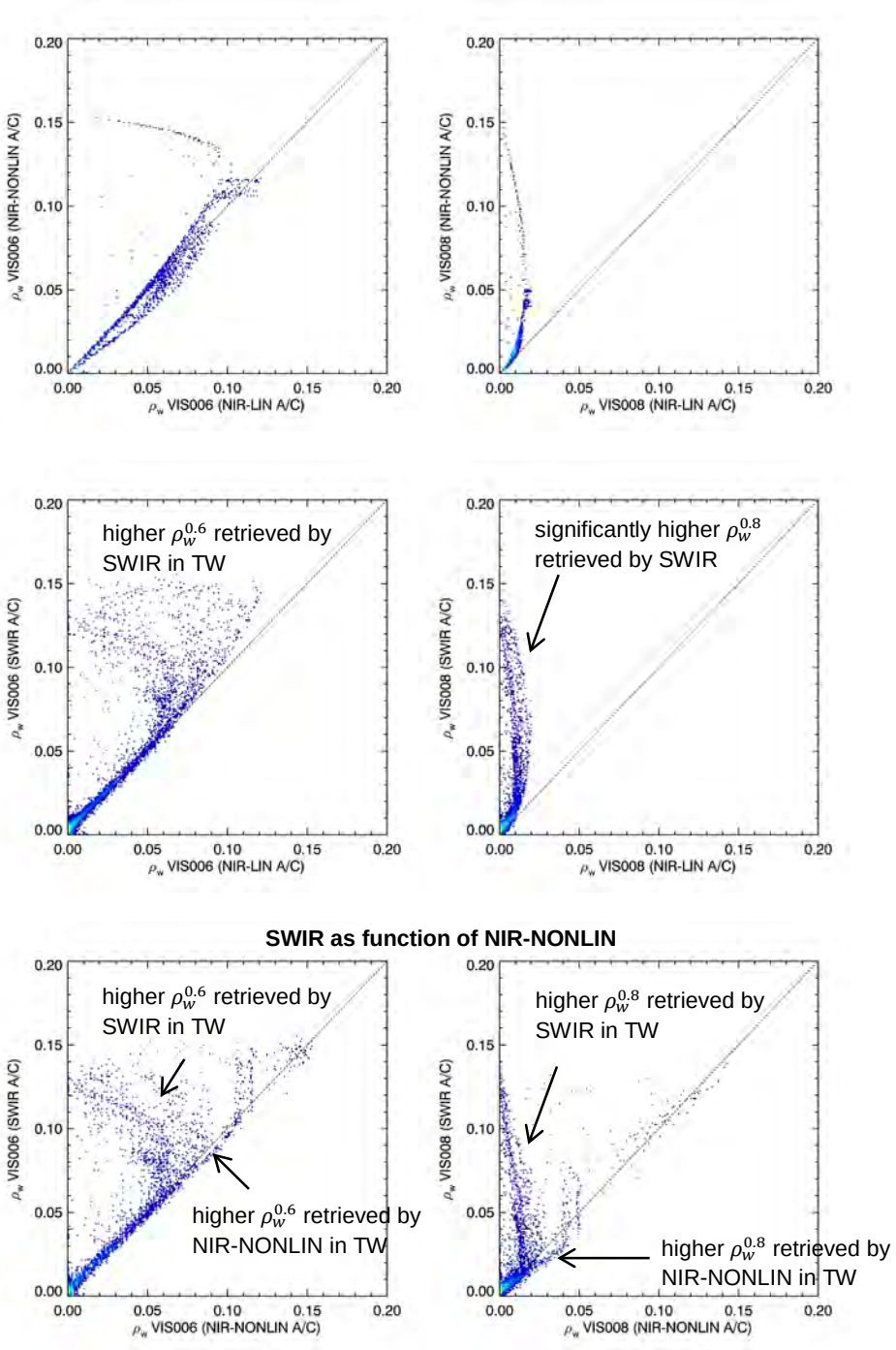

Figure 8 Comparison of the water reflectances in the VIS0.6 (left) and VIS0.8 (right) channels for the Amazon River plume on 2012-08-03 at 14:15 UTC (Figure 6), using different aerosol corrections in the RBINS prototype processor. Top row: NIR-NONLIN compared to NIR-LIN, middle row: SWIR compared to NIR-LIN, and bottom row: NIR-NONLIN compared to SWIR. The dashed line shows the 1:1 line.

5.1.2.6 Processing grid

The assumption of a spatially invariant aerosol in the aerosol correction of (G. Neukermans et al. 2009; G. Neukermans, Ruddick, and Greenwood 2012) cannot be valid over the whole SEVIRI disk. For processing, the disk is therefore subdivided in Aerosol Regions (AR) where a single aerosol type is representative, and can be determined from the image when enough cloud-free pixels are available. These AR are stored in a LUT with for each pixel the AR identifier and distance to the AR centre. This construction allows for testing new or updating the AR configurations without changing the processor code.

The optimal AR configuration might need to be updated based on the SEVIRI data itself, and may likely be equal-area based. The distribution of AR has to be chosen to have a sufficiently large number of clear water pixels in each cell for the aerosol type determination, while still constraining the spatial extent so assuming a single aerosol type per AR is realistic. A cut-off at high viewing zenith angles will need to be determined, as a number of problems will arise concerning aerosol type and water reflectance retrieval:

- the spatial coverage of a single pixel and the variation in the multiple scattering aerosol reflectance will increase,
- the number of pixels in ARs with fixed spatial extent will decrease,
- and at a certain viewing zenith angle the SEVIRI pixel will no longer contain any information on the water reflectance (due to water surface and atmospheric reflectance).

A first version of the AR grid will be using a regular grid of 16x16 or 32x32 regions (Figure 9), this gives zones of 232x232 or 116x116 pixels for a SEVIRI L1.5 file of 3712 by 3712 pixels.

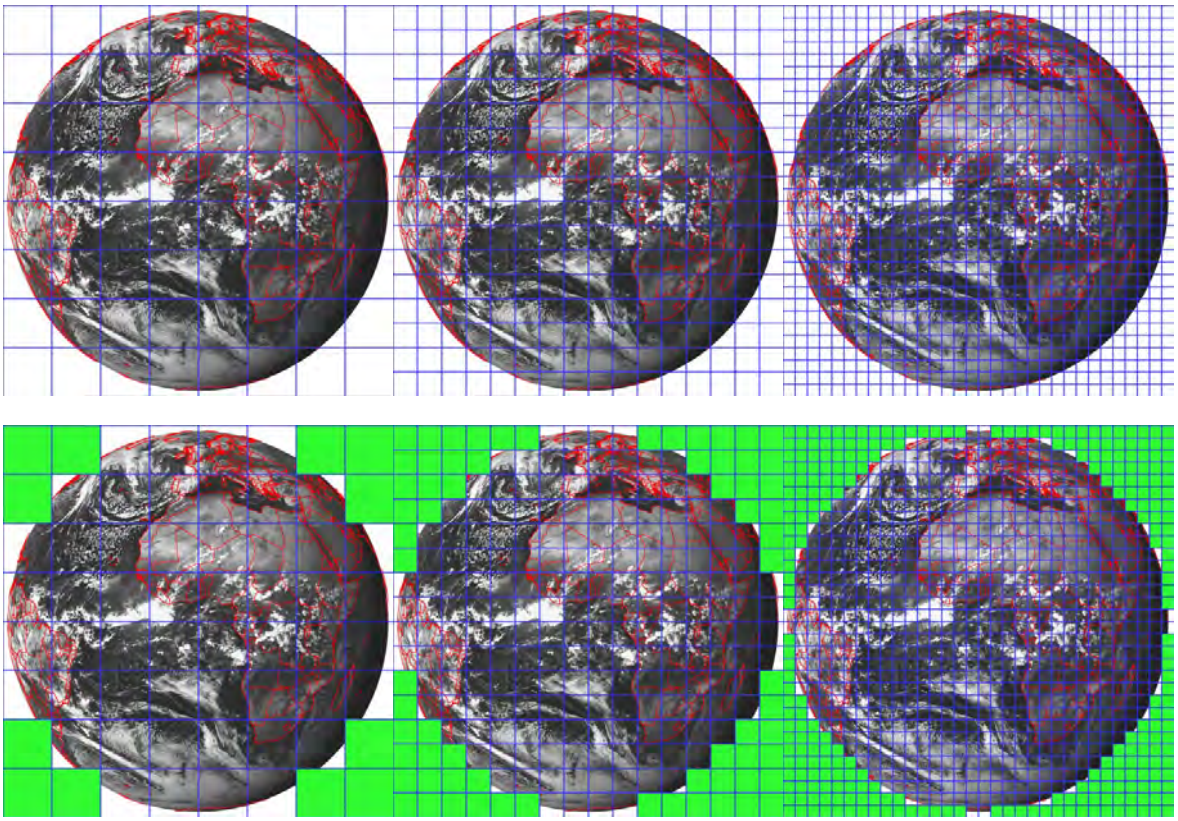

Figure 9 The regular grid of Aerosol Regions in the SEVIRI full disk (blue lines), from left to right: 8x8, 16x16 and 32x32 zones, giving AR of 464x464, 232x232 or 116x116 pixels. The lower figures show the AR that lie >50% outside the disk in green. Those cells do not have to be processed, similarly, cells with 100% land cover do not have to be processed. Country borders are drawn in red. The background is the MSG-2 full disk VIS0.6 top of atmosphere radiance on 2009-04-14 at 14:00.

5.1.2.1 Aerosol Climatology

A fall-back climatology of angstrom exponents will be constructed from the SEVIRI archive itself, containing values for each time-step (15 minutes) per month. At the start of processing, the climatology will contain white aerosols (epsilon = 1, angstrom exponent = 0). For each AR in the processed image, the number of clear-sky clear-water pixels (Nobs) will be compared to a required number of pixels (Nmin) to allow for a robust linear regression to determine the angstrom exponent:

If Nobs >= Nmin, the angstrom exponent is computed for this AR in this image, and the climatology is updated. The time of the last update, the total number of pixels and the weighted mean angstrom exponent is tracked in the climatology.

If Nobs<Nmin, the aerosol exponent is not computed from the image, but the value from the climatology is retrieved and used in the aerosol correction.

Option: If Nobs<Nmin, and enough neighbouring AR have a valid image derived angstrom exponent, the neighbouring angstrom exponents are interpolated to the current AR by distance weighting. Otherwise the climatological fall-back is used.

5.2 Algorithm validation

Full validation of the atmospheric correction algorithm will be possible only at a later stage, after the processor has been developed. At the present stage, algorithm validation is limited to comparison of the Rayleigh Look Up Table (LUT) proposed by HYGEOS for the operational processor, compared to similar LUT used by RBINS in a prior research-oriented processor. This work is in progress and will be reported in an update of this ATBD.

5.3 Uncertainties

An estimate of the uncertainties for water reflectance products arising from the assumption of constant aerosol type, the linear water reflectance model (when used at low reflectance) and the digitisation of TOA SEVIRI data was provided in the feasibility study of (G. Neukermans et al. 2009). This approach needs to be revisited in the light of improvements made during the present study and the temporal averaging proposed by (Q. Vanhellemont, Neukermans, and Ruddick 2014). This work is in progress and will be reported in an update of this ATBD.

5.4 Quality flagging

Each pixel will have an associated product confidence flag (PCD) which will be raised for pixels not passing the following quality checks:

- not a water pixel (according to land and cloud masks)
- $\rho_w^6 < 0$ or $\rho_w^8 < 0$
- ρ_w^6 and ρ_w^8 deviate more than 0.005 from the used marine model
- $\theta_v > x°$ > (65-70), giving large uncertainties due to the large pixel size, and high ratio of atmospheric path signal to water signal
- $\theta_s > x°$ (80°), giving large uncertainties due to low illumination, and high ratio of atmospheric path signal to water signal

The optimal thresholds for these tests will be finalised after the Product Validation task.

Alternatively, if the uncertainty estimates can be established with sufficient reliability it may be possible to have a single test for the PCD according to whether the relative uncertainty for the water reflectance exceeds a certain threshold. At the present state of the art (including for operational missions such as OLCI and VIIRS) the estimate of uncertainties for water reflectance products is not mature enough to reduce a PCD flag to a simple test on relative uncertainty.

L2W parameters will be computed for pixels with the Rrs PCD raised, but they will not be used in L3 compositing or time-series analysis.

5.5 Adaptation to different SEVIRI sensors

The approach detailed in sections 5.1-5.4 is reasonably generic and may be applied to all SEVIRI sensors, although LUTs, e.g. for the Rayleigh correction, will need to be generated for each MSG platform individually.

5.6 Algorithm limitations and recommendations for future improvements

The sections 5.1-5.4 represent the recommended algorithms to be used in the SEVIRI-WT processor according to best available knowledge at the moment of writing. A few open questions are, however, noted and may lead to further refinements during the course of the project as knowledge evolves:

- The analytical non-linear water reflectance model is recommended for default processing, however the NIR1.6-based approach is expected to give better performance for the most turbid water regions and may also provide calibration or validation data for the non-linear

analytical model. This will be further studied using the results that will be obtained from the processor.

- The NIR1.6-based approach is expected to suffer from noise, although spatial and/or temporal filtering may be improved to remedy this.
- The image by image vicarious calibration approach of (G. Neukermans, Ruddick, and Greenwood 2012) has not been recommended here. However, analysis of the offsets obtained for each aerosol region in the approach of section 5.1.2.1 may shed light on any systematic calibration and/or Rayleigh correction biases.
- Uncertainty estimation is currently not fully studied.
- Analysis of the MSGCLMK cloud mask and comparison with the simpler NIR threshold test for non-water pixels will be continued and may lead to refinement of the pixel identification approach.
- The division of the disk in different Aerosol Regions (AR) is currently defined as a regular grid. The AR definition is generic and different configurations (varying grid size, equal area) will be tested after processor development.

6 Standardisation of water reflectance products

The output of the atmospheric correction algorithm described in section 4 consists of instantaneous, band-weighted, directional water-leaving radiance reflectance for the VIS0.6 and VIS0.8 bands of the specific SEVIRI sensor with products available for at the (low) VIS0.6/VIS0.8 native resolution, termed hereafter Low Resolution (LR). Products at the resolution of the HRV ("High Resolution Visible") band are described later in section 7 and termed hereafter High Resolution (HR) products. The LR and HR product grids have a resolution which varies with viewing zenith (and, because of the map projection, azimuth) angle.

Use of these atmospheric correction algorithm outputs to estimate water-products may be preceded by a number of "standardisation"[3] steps, including potentially band-shifting to a standard or nominal narrow-band product (to facilitate algorithm development for all SEVIRI sensors), temporal filtering (to reduce noise) and removal of bidirectional effects. Each of these standardisation steps is described in the following subsections and conclusions regarding the implementation are given in section 6.4 and Figure 13.

6.1 Band-shifting

The use of a standard wavelength for the SEVIRI-WT water reflectance product facilitates intercomparison and exploitation of data in a multi-mission context. The SEVIRI sensors onboard MSG-1, -2, -3 and -4 (also called Meteosat-8, 9, 10 and 11) have slightly different spectral response (Figure 10). These differences can be removed, allowing direct intercomparison of products, by appropriate band-shifting of products to a common band.

[3] The term "normalisation" is deliberately avoided here because of the many different meanings given to this term in the ocean colour literature.

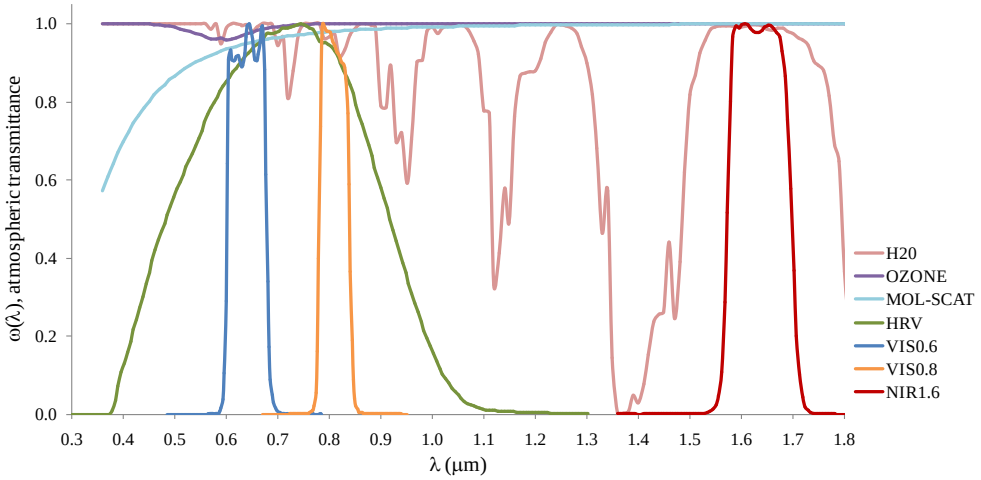

Figure 10 Spectral response function of MSG-1 SEVIRI VIS0.6, VIS0.8 and HRV bands. Normalized spectral response, of the SEVIRI solar channels and two-way atmospheric transmittances for water vapour, ozone and molecular scattering for a vertical atmospheric path and the US standard atmosphere model simulated with LOWTRAN. Reproduced from N2009 using data from (Govaerts and Clerici 2004) for the SEVIRI spectral response function.

If, moreover, the common band is chosen to be very narrow, effectively a single wavelength approach, then the SEVIRI-WT water reflectance product may be used as input to algorithms designed outside the SEVIRI-WT project, typically calibrated/validated with a central or single wavelength approach.

However, it is important that use of a common, narrow wavelength approach for the SEVIRI-WT processor output does not introduce unacceptable uncertainties into the product compared to the use by an algorithm of a band-weighted reflectance product. The uncertainty introduced by estimating a standardised narrow band reflectance from the band-integrated reflectance product is therefore analysed in this section.

Following (G. Neukermans, Ruddick, and Greenwood 2012), the band-integrated above-water marine reflectance, the output product of the atmospheric correction, is defined as:

$$\rho_w^{ij} = \pi \frac{\int \omega_{ij}(\lambda) L_w^{0+}(\lambda) d\lambda}{\int \omega_{ij}(\lambda) E_d^{0+}(\lambda) d\lambda} \qquad 28$$

where $\omega_{ij}(\lambda)$ is the sensor response function for the band i on platform MSG-j, $L_w^{0+}(\lambda)$ is the water-leaving radiance and $E_d^{0+}(\lambda)$ is the downwelling irradiance.

The narrow band remote sensing reflectance is defined as:

$$Rrs(\lambda_i) = \frac{L_w^{0+}(\lambda_i)}{E_d^{0+}(\lambda_i)} \qquad 29$$

We seek a linear relationship between the band-integrated and narrow band parameters of the form:

$$Rrs(\lambda_i) = a_{ij}\rho_w^{ij}/\pi + b_{ij} + e_{ij} \qquad 30$$

where a_{ij} and b_{ij} are the linear regression coefficients and e_{ij} is the error term. In the case of a infinitesimally narrow sensor response function, $\omega_{ij}(\lambda) = \delta(\lambda_i)$, where δ is the Dirac delta function, and trivially $a_{ij} = 1$, $b_{ij} = 0$ and $e_{ij} = 0$. For a real sensor response function and a water target with some spectral variability of reflectance, then a_{ij} will be close to 1.0, b_{ij} should be very close to zero

and the error term will represent the effective difference between a band-weighted and a narrow band approach.

If necessary an alternative non-linear, e.g. polynomial, function could be used instead of this linear form, but results (shown later) indicate that this linear formulation is sufficient.

6.1.1 Method for analysing narrow band approach

The approach outlined above is tested and calibrated by use of the seaborne data acquired by RBINS using a three radiometer abovewater instrument system, as described by (KG Ruddick et al. 2006).

TriOS measurements of sky radiance, Lsky, sea radiance, Lsea, and downwelling irradiance, Ed, were collected between April 2007 and April 2015, with a total number of stations N=912 located in the southern North Sea, French Guyana and the Mediterranean Sea. The spectra, provided at a spectral resolution of 2.5 nm for wavelengths ranging from 350 nm to 900 nm (221 values by scan), were quality controlled and processed as described here:

- Ed-sensor inclination lower than 5 degrees (as in (KG Ruddick et al. 2006))
- Spectra where spectral jump occurred, or high time variability between consecutive scans was observed, have been rejected (as in (KG Ruddick et al. 2006))
- Any spectra with negative values were rejected
- At each station, the 5 consecutive Lsea and Lsky spectra where used to estimate the water-leaving radiance following:

  $$Lw = Lsea - \rho_F \times Lsky$$

  where ρ_F is the Fresnel reflectance.
- Lw and Ed spectra were convoluted with SEVIRI response functions, following Eq. (28), which yielded SEVIRI reflectance, denoted by SEVIRI-*Rrs*, with $Rrs^{i=1,2} = \rho_w^{i=1,2}/\pi$, i referring to SEVIRI bands VIS0.6µm and VIS0.8µm. These spectra were obtained for each of the four SEVIRI MSG-versions. Note that the direct convolution of Lw with SEVIRI response function was allowed due to the linear relationship between Lw and the sum of Lsea and $\rho_F \times$ Lsky
- Eq. (29) was applied to Lw and Ed spectra yielding narrow-band reflectance spectra, $Rrs^{j=1,\dots,221}$
- Narrow band reflectance spectra where the standard deviation (over the 5 consecutive scans) to the mean value at 750 nm exceeded 10% have been rejected, to avoid any variability during reflectance measurement induced by variable sky conditions or water mass fronts; this led to a total number of 329 reflectance spectra
- Linear regression analysis was applied to SEVIRI-Rrs^i and narrow-band Rrs^j, to establish the coefficients a_i, b_i and e_i (of Eq. 3) for the narrow band j corresponding to the lowest mean absolute percentage error, $MAPE^j$ defined by:

  $$MAPE^j = \frac{1}{N}\sum_{i=1}^{N} abs(SEVIRI\ Rrs^i - narrow\ band\ Rrs^j)/SEVIRI\ Rrs^i \qquad 31$$
- Correlation coefficient and root mean square error, RMSE, were also calculated for each narrow band:

  $$RMSE^j = \sqrt{\frac{\sum_{i=1}^{N}(SEVIRI\ Rrs^i - narrow\ band\ Rrs^j)^2}{N}} \qquad 32$$

5.1.2. Results for uncertainty of standardised narrow band approach

Figure 11 and Figure 12 present scatterplots of (x-axis) ρ_w^i/π against (y-axis) $Rrs(\lambda_i)$ for the VIS0.6 and VIS0.8 bands (for each SEVIRI sensor) and the linear regression statistics giving slope, a_i, intercept, b_i, RMS error, e_i and correlation coefficient, r^2. These metrics are also reported in Table 2.

The lowest relative errors (<1.8%) are found between reflectance at the narrow band 640 nm and SEVIRI MSG-1, MSG-2, MSG-3 and MSG-4 VIS0.6 bands. Therefore, the narrow band 640 nm is taken as one standard band for SEVIRI-WT products. For band VIS0.8, reflectance at the narrow band 785 nm gives the best results for all SEVIRI MSG-versions, with mean relative error < 1%.

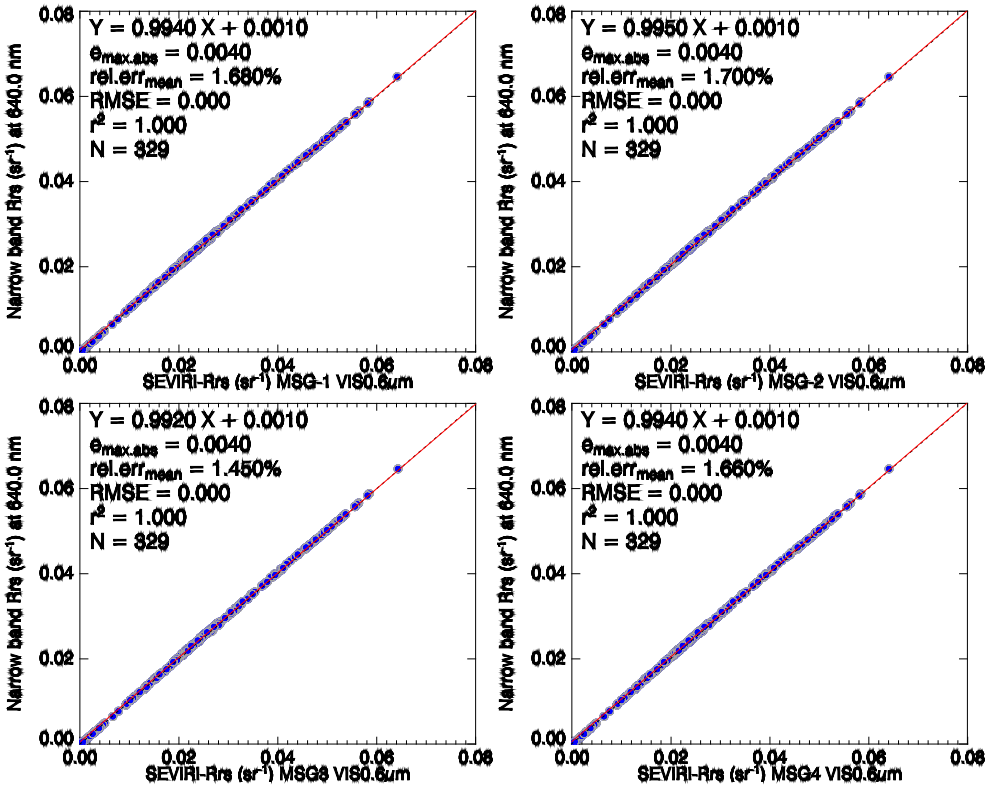

Figure 11: Rrs at the narrow bands around 640 nm that fit the best SEVIRI VIS0.6µm reflectance, for the four SEVIRI MSG-versions.

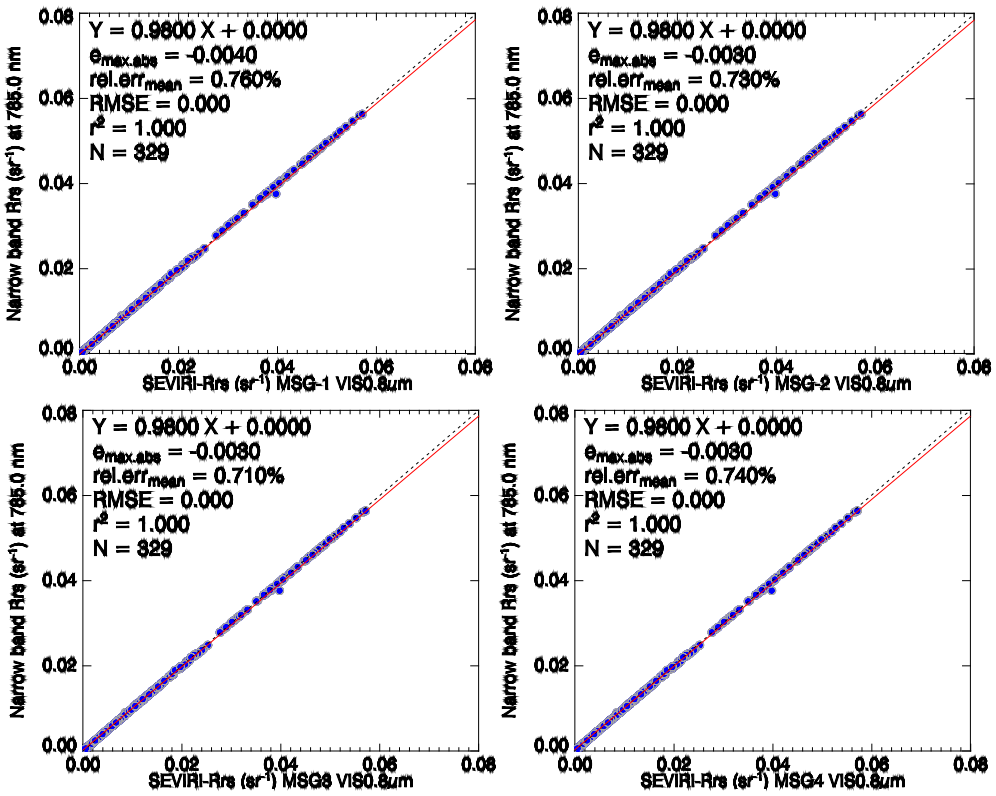

Figure 12: Rrs at the narrow bands around 809 nm that fit the best SEVIRI VIS0.6µm and VIS0.8µm reflectance, for the four SEVIRI MSG-versions.

Wavelength	Regression	MSG-1	MSG-2	MSG-3	MSG-4
$\lambda_1 = 640nm$	a_{1j}	0.994	0.995	0.992	0.994
	b_{1j}	5.175E-04	5.152E-04	5.240E-04	5.164E-04
	e_{1j}	5.059E-04	5.077E-04	5.102E-04	5.033E-04
	r_{1j}^2	1.000	1.000	1.000	1.000
$\lambda_2 = 785nm$	a_{2j}	0.980	0.980	0.980	0.980
	b_{2j}	2.532E-04	2.185E-04	2.218E-04	2.199E-04
	e_{2j}	5.359E-04	5.282E-04	5.193E-04	5.347E-04
	r_{2j}^2	1.000	1.000	1.000	1.000

Table 2 Regression analysis summary for standardised wavelengths.

It is noted that the nominal wavelength 785nm is quite different from the central wavelength of this SEVIRI band, generally given as 810nm. This is because the longer wavelengths within this broad band contribute less to the water-leaving radiance. The change in nominal wavelength with respect to the original project plans (including URD and PDD) will have no real impact on applications, which can be written for 785nm or 810nm interchangeably.

6.1.2 Results for uncertainty of standardised narrow band approach

Since the relative error caused by the band-shifting approach is <1% it can be safely ignored in the full uncertainty estimate for the Rrs products.

6.1.3 Implementation

On the basis of the results of section 6.1.2 it is decided to implement the narrow band approach for L2R product output.

6.2 Temporal filtering

Since the algorithms to be applied later, e.g. for turbidity, have some non-linearity at high reflectance it is clearly preferable to apply any temporal averaging to reflectance products rather than averaging of the final L2W products in post-processing.

The first use of SEVIRI data for suspended matter-related applications (G. Neukermans et al. 2009) showed an important impact of digitisation of data at the top of atmosphere, which corresponds to high noise for SPM products in clear waters. The impact of sensor noise is quite similar to the digitisation noise and the two are presumably related by design since there is no advantage to digitise data to a level that is much finer than the noise specification of the instrument. In a follow-up paper (G. Neukermans, Ruddick, and Greenwood 2012) showed that temporal smoothing of data provided more acceptable time series (their Fig 8). A five-image mean averaging of 15-minute data was adopted by (Q. Vanhellemont, Neukermans, and Ruddick 2014) and found to give good reduction of noise, while not affecting the real signal, in this case variability of SPM caused by tidal dynamics.

Provided that noise (and digitisation) can be expected to have a random, unbiased impact on the top of atmosphere radiance, a N_{ave}-image mean average seems to be an appropriate temporal filter and should provide reduction of noise to a factor $\sqrt{N_{ave}}$. The duration over which any filtering is applied should be significantly less than the time scale of processes that need to be observed, typically 6 hours for the case of tidal or diurnal processes.

It seems appropriate to fix the upper limit for the duration of a temporal filtering to 1 hour, i.e. 30 minutes before and after the image being processed, to avoid undesirable smoothing of natural processes associated with tides and/or the diurnal cycle of light and heat. The resulting values of N_{ave} and $1/\sqrt{N_{ave}}$ are summarised in Table 3.

Δt	N_{ave}	$1/\sqrt{N_{ave}}$
15 min (standard)	5	0.45
5 min (Rapid Scan Service)	13	0.28
2.5 min (MTG Rapid Scan Service)	25	0.20

Table 3 Suggested number of images to be used for time-averaging of reflectance data and corresponding noise reduction factor according to the temporal resolution, Δt , of the raw SEVIRI data.

In a Near-Real-Time (NRT) context, the use of images in the future of the image being processed will delay data production. According to the User Requirements (D1.1), it seems that a 30 minute delay (in addition to the normal processing time) will not be critical for most applications. If this delay is found to be a critical problem for any application, N_{ave} could be reduced, perhaps considering output of a new "unfiltered" user product.

6.3 Bidirectional effects

It is well known (Morel and Gentili 1993) that the water reflectance depends not just on water inherent optical properties but also on the illumination conditions, particularly the sun zenith angle, and the viewing geometry. For Case 1 waters, where the water IOPs can be considered to vary only as function of one parameter, e.g.. chlorophyll a concentration, a reliable and well-accepted approach has been suggested by (Morel and Gentili 1996) and has been adopted, via a "f/Q" correction, for many ocean colour processors, giving a "normalised" water reflectance product.

In the turbid waters for which the SEVIRI-WT processor is developed the state of bidirectional correction algorithms is less mature, although there has been research studies (Loisel and Morel 2001; Park and Ruddick 2005) for geometries typical of polar-orbiting satellites. interestingly, (Q. Vanhellemont, Neukermans, and Ruddick 2014) demonstrated that sensors on geostationary platforms will require consideration of a much wider range of illumination and viewing geometries, including for some regions/times of day side or slightly forward scattering geometries.

In view of the lack of consensus regarding bidirectional corrections for turbid waters, it is proposed that the SEVIRI-WT processor provide directional water reflectance products, thus leaving the choice of any bidirectional corrections to downstream algorithms, if and when such corrections are considered to be mature.

6.4 Summary of standardisation of reflectance products

The steps of band shifting and temporal averaging described in sections 6.1 and 6.2 are linear operators which can be implemented in the order depicted in Figure 13.

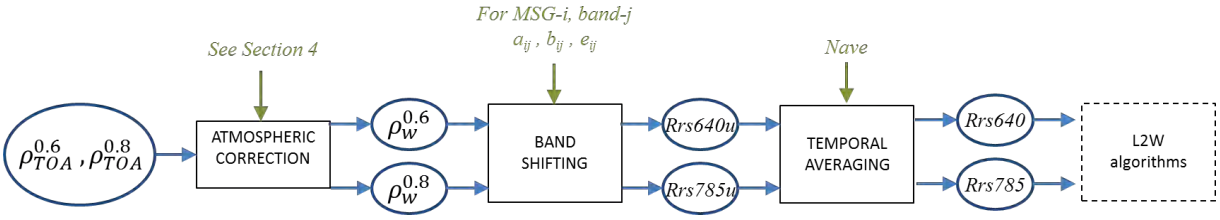

Figure 13 Overview of steps between atmospheric correction and final L2R (radiometric) water reflectance products to be used subsequently in the L2W (water) products. Green arrows show configuration and calibration parameters. The band-weighted water reflectance, ρ_w and the instantaneous unfiltered remote sensing reflectances, Rrs640u and Rrs785u, are internal, intermediate products. The temporally averaged remote sensing reflectances, Rrs640u and Rrs785u, are final products for users and are used as inputs for other L2W products to be generated for users.

7 Water reflectances at HRV band spatial resolution

The User Requirements Document (URD, D1.1) stressed the limitation of spatial resolution of SEVIRI for the VIS0.6 and VIS0.8 bands and gives high priority to exploitation of the HRV band to achieve a threefold improvement in spatial resolution. Considering the very broad nature of the HRV band (Figure 10), it not considered appropriate to perform an atmospheric correction of this data according to the "usual" ocean colour methodology (Gordon and Morel 1983) whereby the top of atmosphere (TOA) signal is corrected for gaseous absorption and then corrected for Rayleigh scattering and aerosol scattering and for two way diffuse atmospheric transmittance. The spectral variation of Rayleigh scattering and water reflectance within the HRV band, as well as the lack of a clear reference wavelength for extrapolation of aerosol reflectance would give severe problems for such an approach. Rather the approach adopted here, following that of (G. Neukermans, Ruddick, and Greenwood 2012), is to assume that the spatial variation of the HRV reflectance at TOA over a Low Resolution pixel is caused by spatial variability of the water reflectance, slightly attenuated by the atmospheric transmittance. i.e. spatial variability of atmospheric reflectance within the LR pixel is assumed negligible.

The products that will be generated represent geophysically the VIS0.6 and VIS0.8 band reflectances and not the HRV-band reflectance. I.e. As far as users are concerned, these are the same products as those generated for the low resolution (LR) data, but they are simply provided on a high resolution (HR) grid. The approach is also described in (Vanhellemont et al, 2015) as "pan-sharpening", using terminology more common for land remote sensing applications with panchromatic spectral bands.

$$\rho_{w(HR)}^{0.6} = \rho_{w(LR)}^{0.6} + f_{0.6}(\hat{\rho}_w^{HRV}) \qquad 33$$

where $\rho_{w(HR)}^{0.6}$ is the band-weighted reflectance on the HR grid, $\rho_{w(LR)}^{0.6}$ is the band-weighted reflectance on the LR grid, $f_{0.6}$ is a suitable function to convert HRV-band water reflectance into 0.6µm band reflectance and $\hat{\rho}_w^{HRV}$ is the spatial anomaly of the HRV band-weighted water reflectance over the LR pixel. i.e.

$$\hat{\rho}_w^{HRV} = \rho_{w(HR)}^{HRV} - \bar{\rho}_{w(LR)}^{HRV} \qquad 34$$

where $\bar{\rho}_{w(LR)}^{HRV}$ is the spatial average of the HRV band water reflectance for a LR pixel.

7.1 Effective atmospheric transmittance at HRV band

To transfer the HRV band reflectance from TOA to water reflectance we define $T_{0,v}^{HRV}$ as the effective two-way diffuse atmospheric transmittance for the HRV band

$$T_{0,v}^{HRV} = \frac{\hat{\rho}_{TOA}^{HRV}}{\hat{\rho}_{w}^{HRV}} \quad 35$$

In (G. Neukermans, Ruddick, and Greenwood 2012) $T_{0,v}^{HRV}$ was modelled from simulations based on the impact at TOA of typical in situ water reflectance spectra and the formulation:

$$T_{0,v}^{HRV} = T_{0,v}^{0.6}\alpha^{m/2} \quad 36$$

was proposed where m is the two-way airmass:

$$m = \frac{1}{Cos\theta_0} + \frac{1}{Cos\theta_v} \quad 37$$

for sun and viewing zenith angles θ_0 and θ_v, and $T_{0,v}^{0.6}$ is the two-way diffuse atmospheric transmittance calculated for the 0.6µm band.

In principle, α will depend on the spectral response function of the 0.6µm band and the HRV band for each MSG platform. In practice for the present contract it is proposed to accept the calibration of (G. Neukermans, Ruddick, and Greenwood 2012) for all platforms, giving $\alpha_1 = \alpha_2 = \alpha_3 = \alpha_4 = 0.96$.

7.2 Converting HRV band to VIS0.6 and VIS0.8 bands

Implementation of the HRV-sharpening approach also requires a method for converting the HRV band-weighted water reflectance spatial anomaly to 0.6µm and 0.8µm band-weighted reflectances via functions $f_{0.6}$ and $f_{0.8}$. It is important to note here that the HRV water reflectance data is available only as a spatial anomaly and not as the HRV water reflectance itself, unless the spatial mean of the HRV water reflectance is obtained from the VIS0.6 band-weighted reflectance by use of a model. Three approaches have been considered to deal with this conversion of HRV spatial anomaly into spatial anomalies for the VIS0.6 and VIS0.8 bands as outlined in the following three subsections.

7.2.1 Converting HRV to VIS0.6 and VIS0.8 reflectance – linear approach

In (G. Neukermans, Ruddick, and Greenwood 2012) this was achieved by a simple linear function:

$$f_{0.6} = K\hat{\rho}_{w}^{HRV}$$

where $K = 1/0.71$ was calibrated from in situ reflectance measurements. This approach has the advantage of simplicity and should give good performance for low and moderate water reflectances. However, it is now clear that this relationship between VIS0.6 and HRV reflectance will not remain linear at high reflectance because the HRV band will saturate faster than the 0.6µm band as shown in (Vanhellemont and Ruddick, 2015).

7.2.2 Converting HRV to VIS0.6 and VIS0.8 reflectance – non-linear approach

An approach which gives good representation of the non-linearity relationship between HRV and VIS0.6 water reflectance at high reflectance is to use the same non-linear reflectance model as for turbid water atmospheric correction and for L2W/S products, by relating the HRV band water reflectance first to Turbidity and thence to 0.6µm band water reflectance. Thus, using the model of Annex A,

$$\rho_{w(LR)}^{HRV} = \rho_{w(LR)}^{0.6}\frac{A_{T(0.6)}}{A_{T(HRV)} + \rho_{w(LR)}^{0.6}\left(A_{T(0.6)}/C_{HRV} - A_{T(HRV)}/C_{(0.6)}\right)}$$

or, using the band-shifted formulation for the 0.6µm band,

$$\rho_{w(LR)}^{HRV} = \pi Rrs_{(LR)}^{640} \frac{A_{T(640)}}{A_{T(HRV)} + \pi Rrs_{(LR)}^{640} \left(A_{T(640)}/C_{HRV} - A_{T(HRV)}/C_{(640)}\right)}$$

Next the water reflectance at the HRV band on the HR grid is obtained simply by adding the spatial anomaly of the HRV band at TOA, adapted by the atmospheric transmittance:

$$\rho_{w(HR)}^{HRV} = \rho_{w(LR)}^{HRV} + \frac{\hat{\rho}_{TOA}^{HRV}}{T_{0,v}^{HRV}}$$

and finally this is converted back to the band-weighted 0.6µm band by:

$$\rho_{w(HR)}^{0.6} = \rho_{w(HR)}^{HRV} \frac{A_{T(HRV)}}{A_{T(0.6)} + \rho_{w(HR)}^{HRV}\left(A_{T(HRV)}/C_{0.6} - A_{T(0.6)}/C_{(HRV)}\right)}$$

or the band-shifted 640nm band by:

$$Rrs_{(HR)}^{640} = \frac{\rho_{w(HR)}^{HRV}}{\pi} \frac{A_{T(HRV)}}{A_{T(640)} + \rho_{w(HR)}^{HRV}\left(A_{T(HRV)}/C_{640} - A_{T(640)}/C_{(HRV)}\right)}$$

The original simple linear formulation of (G. Neukermans, Ruddick, and Greenwood 2012) can be obtained from the low reflectance limit of $\rho_w^{0.6} \ll C_{0.6}$ and $\rho_w^{HRV} \ll C_{HRV}$, which gives $\rho_{w(HR)}^{0.6} = K\rho_{w(HR)}^{HRV}$, where $K = A_{T(HRV)}/A_{T(0.6)}$.

7.2.3 Converting HRV to VIS0.6 and VIS0.8 reflectance – locally-linear approach

The approach of section 7.2.2 is theoretically well-founded, provided that the underlying reflectance model (Annex A) is valid at high reflectance. However, the approach is relatively complex because of the need for the intermediate step of estimating turbidity. Moreover at high reflectance there may be problems associated with exceedance of the maximum HRV or VIS0.6 band water reflectance allowable in the underlying reflectance model. An intermediate locally-linear approach is therefore proposed here which should give better performance at high reflectance than the linear approach of section 7.2.1 but avoiding the complexity of the fully non-linear approach of section 7.2.2. It is, thus, assumed that the spatial anomaly of the water reflectance at the VIS0.6 (or VIS0.8) band can be obtained from the spatial anomaly of the HRV water reflectance by the derivative of the function relating the two reflectances, evaluated at the VIS0.6 reflectance:

$$f_{0.6} = \frac{d\rho_w^{0.6}}{d\rho_w^{HRV}} \hat{\rho}_w^{HRV}$$

where the derivative can be easily calculated from the analytical reflectance model as:

$$\frac{d\rho_w^{0.6}}{d\rho_w^{HRV}} = \frac{A_{T(0.6)}A_{T(HRV)}}{\left\{A_{T(0.6)} + \rho_w^{HRV}\left(A_{T(HRV)}/C_{0.6} - A_{T(0.6)}/C_{(HRV)}\right)\right\}^2}$$

this has the low reflectance limit of $d\rho_w^{0.6}/d\rho_w^{HRV} = A_{T(HRV)}/A_{T(0.6)}$

and the high reflectance limit as $\rho_w^{HRV} \to C_{HRV}$ of $d\rho_w^{0.6}/d\rho_w^{HRV} = \left(A_{T(HRV)}/A_{T(0.6)}\right) * \left(C_{0.6}/C_{(HRV)}\right)^2$.

If the HRV-sharpening is combined with band-shifting then:

$$\frac{dRrs^{640}}{d\rho_w^{HRV}} = \frac{1}{\pi}\frac{A_{T(640)}A_{T(HRV)}}{\left\{A_{T(640)} + \rho_w^{HRV}\left(A_{T(HRV)}/C_{640} - A_{T(640)}/C_{(HRV)}\right)\right\}^2}$$

The locally-linear approach is thought to be sufficiently accurate for representing the relationship between the HRV and VIS0.6 spatial anomalies and combines simplicity with the future perspective that it might be possible to calculate the local derivative $d\rho_w^{0.6}/d\rho_w^{HRV}$ from the image data itself, e.g. by use of a spatial kernel of sufficient size around the target pixel – see Fig 2b of (Vanhellemont and Ruddick, 2015).

For the SEVIRI-WT processor it is therefore proposed to use the locally-linear approach for relating the HRV reflectance anomaly to the VIS0.6 (and VIS0.8) water reflectance anomalies.

With the locally-linear approach, because of the high reflectance non-linearity which affects differently the HRV and 0.6 bands, the final results will depend slightly on whether band-shifting is performed before or after HRV sharpening. With the future perspective of potentially estimating the derivative from image data **it seems more appropriate to perform HRV-sharpening before band-shifting**. This implies the need for coefficients $A_{T(0.6)}, A_{T(0.8)}, C_{(0.6)}, C_{(0.8)}$ for all MSG platforms in addition to the coefficients $A_{T(HRV)}, C_{HRV}$ required for the approach with HRV-sharpening after band-shifting.

These coefficients are provided in Table 4 on the basis of a regression analysis using the RBINS/TRIOS in situ data described in more detail in section 8.1.

T-algo coefficients	MSG1			MSG2		
W.bands	HRV	0.6µm	0.8µm	HRV	0.6µm	0.8µm
A_T	515.53	231.12	1841.46	512.69	231.34	1831.1
(B_T)	0.19	-0.07	-0.25	0.19	-0.07	-0.24
C_T	0.1994	0.16387	0.20862	0.19925	0.1639	0.20853
R^2	74.9	91.1	96.2	74.9	91.1	96.2
T-algo coefficients	FM3			FM4		
W.bands	HRV	0.6µm	0.8µm	HRV	0.6µm	0.8µm
A_T	512.39	226.33	1833.71	512.95	230.77	1830.34
(B_T)	0.19	-0.07	-0.24	0.19	-0.07	-0.24
C_T	0.19932	0.16295	0.20853	0.19927	0.16376	0.20853
R^2	74.9	91.0	96.2	74.9	91.1	96.2

Table 4 Coefficients required for HRV sharpening for each MSG platform, as well as the offset, BT, and regression coefficient for the analysis (see also section 8.1). All the coefficients given here are for band-weighted (not band-shifted) wavelengths.

7.3 HRV-sharpening – summary of proposed implementation

As conclusion of the analysis and approaches considered in section 7.1 and 7.2, we summarise here the proposed implementation of HRV-sharpening.

$$\rho_{w(HR)}^{0.6} = \rho_{w(LR)}^{0.6} + \left(\frac{1}{T_{0,v}^{0.6}\alpha^{m/2}}\right) * \left(\frac{d\rho_w^{0.6}}{d\rho_w^{HRV}}\right) * \hat{\rho}_{TOA}^{HRV}$$

where the first bracketed factor represents atmospheric transmittance and is given in section 7.1 and the second bracketed factor represents the different spatial anomalies of water reflectance at the HRV and VIS0.6 bands and is given in section 7.2.3. The VIS0.8 band is treated in an analogous way. The coefficients to calculate $\frac{d\rho_w^{0.6}}{d\rho_w^{HRV}}$ and $\frac{d\rho_w^{0.8}}{d\rho_w^{HRV}}$ are taken from Table 4. To give a rough idea for checking subsequent implementation, the value of $\frac{d\rho_w^{0.6}}{d\rho_w^{HRV}}$ varies from about 2.4 at low reflectance to about 0.28 at high reflectance.

The flowchart showing the steps in generation of the HR water products is depicted in Figure 14. The HR products are defined to be geophysically identical to the LR products, but are simply provided on a higher resolution grid (with a different value for the uncertainty estimate). Since all subsequent steps (band shifting, temporal averaging, L2W algorithms) are identical, whether applied to HR or LR data, the same product name is used and the algorithms described in the following sections are applied in exactly the same way to LR and HR products.

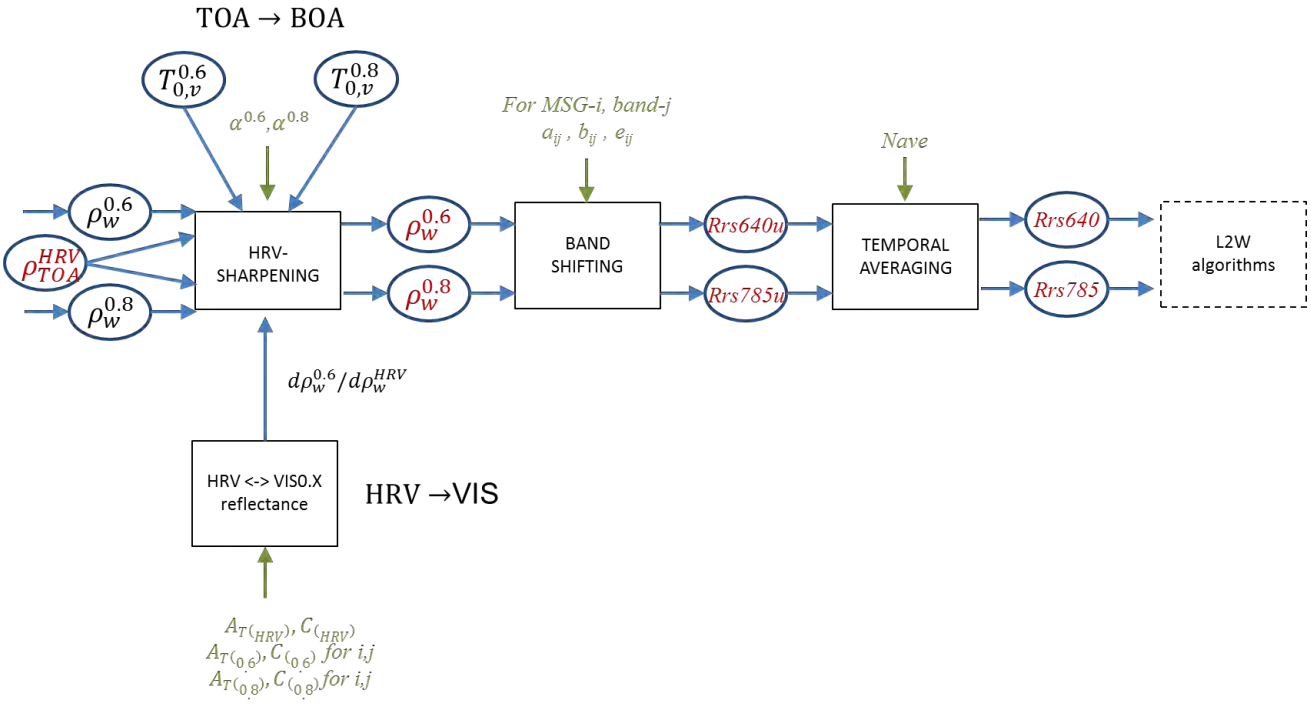

Figure 14 Overview of steps for the high resolution (HR) products. LR water reflectance products obtained from the atmospheric correction described in section 4 are shown in black. HR products are given in red. After the HRV-sharpening step, all reflectance standardisation steps (section 6) and L2W algorithms (sections 8, 9 and 10) are identical whether applied to HR or LR products. Green arrows show configuration and calibration parameters.

8 Suspended Matter-related water products (L2W/S)

The products for **turbidity (T)**, **Suspended Particulate Matter concentration (SPM)** and **Particulate backscatter at 640nm (bbp640)** are closely inter-related and derived essentially from the same water reflectance (Rrs) input.

In prior work algorithms were derived for SPM (G. Neukermans et al. 2009) and TUR (G. Neukermans, Ruddick, and Greenwood 2012) using the same underlying model (Nechad, Ruddick, and Neukermans 2009; Nechad, Ruddick, and Park 2010), but with independent calibrations using in situ data for SPM and TUR respectively. That work is revisited here and refined by adoption of a single "master" inherent optical property (IOP), namely turbidity (or side-scattering at 860nm), from which all other properties, SPM and bbp640, are derived using simple conversion factors. This new formulation is similar to that proposed by (Doerffer 2006) for the gravimetric MERIS Total Suspended Matter product, which is derived from the optical scattering coefficient at 443nm, bp443, and follows the approach of (Dogliotti et al. 2015) who demonstrate the robustness of turbidity retrieval for particles with unknown scattering phase function.

The choice of which IOP should be used as master IOP was made after the following considerations:

- **Particulate backscatter**, bbp, is considered by many to be the most appropriate scattering IOP, because water reflectance is strongly related to bbp, e.g. via the analytical reflectance models of (Gordon, Brown, and Jacobs 1975; Morel and Prieur 1977). Most ocean colour theory has been built on the concept of particulate backscatter. However, there are instrumental difficulties in measuring particulate backscatter in turbid waters: a) because some commercial instruments are simply not designed to measure for a wide range of values, b) because affordable instruments will typically measure only a single angle or a limited number of angles and integrate from this/these to give the full hemisphere bbp, and c) because most bbp instruments have path lengths that are too long to measure in the most turbid waters (Doxoran, in press). As a consequence there are simply insufficient measurements in turbid waters, coincident with red and/or near infrared water reflectances, for calibration or validation of a bbp640 algorithm.
- **Suspended particulate matter**, SPM, is a gravimetric property, not an optical property. Conversion from optical properties to gravimetric properties adds considerable uncertainty arising from natural variability of mass-specific optical properties (Babin et al. 2003; G. Neukermans et al. 2012). Clearly SPM should not be the "master" product but should be derived from an optical product (Doerffer 2006).
- **Turbidity,** T, when correctly defined as an optical product, e.g. following (ISO 1999; Nechad, Ruddick, and Neukermans 2009), has the advantage over bbp of being by definition a single-angle property. Moreover, many low cost instruments, both laboratory and in-water, are available for measuring turbidity and are being used by various groups, including scientists studying sediment transport. Recent work during the FP7/HIGHROC (NIVA, RBINS, CEFAS, LOV) and BELSPO/TURBINET (RBINS, IAFE) projects has been carried out to harmonise protocols and intercompare methods and instruments for measurement of turbidity, including instruments, like the Seapoint "turbidimeter" used on the CEFAS Smartbuoy network, which do not follow the ISO protocol of 90° scattering at 860nm. Radiative transfer simulations (Dogliotti et al. 2015) show that reflectance is very strongly related to turbidity as well as bbp and is only very weakly dependent on the scattering phase function (for fixed turbidity). One drawback of using turbidity as an IOP is the lack of an absolute calibration in SI units. Turbidimeters are, by definition, calibrated with respect to the chemical reference Formazine rather than a physical reference. This drawback should be removed in the future,

since precise determination of the Volume Scattering Function of a known quantity of Formazine will allow conversion from Formazine Nephelometric Units (FNU) to SI units of scattering (m^{-1}).

Because of the excellent availability of data for algorithm calibration and validation, it is decided to use here turbidity as the master IOP, from which bbp640 and SPM will be directly calculated.

8.1 Turbidity (T)

As noted in the Product Definition Document (D1.2), Turbidity (T) is defined by (ISO 1999) as the ratio of side-scattering at 90° of light with wavelength 860nm to side scattering of the same light by a standard solution of Formazin and is expressed in Formazin Nephelometric Units (FNU).

8.1.1 T Algorithm description

T is estimated from the inputs:

- Rrs640, the remote sensing reflectance at 640nm[4], and the uncertainty estimated for this product
- Rrs785, the remote sensing reflectance at 810nm[1], and the uncertainty estimated for this product
- PCD flag for Rrs640 and Rrs785

The turbidity algorithm of (Nechad, Ruddick, and Neukermans 2009) has been found to give good performance for both low reflectance (linear regime) and high reflectance (non-linear asymptotic or "saturation" regime) and will be adopted here.

The turbidity algorithm is based on the reflectance model of (Gordon et al. 1988), where the relationship between the remote-sensing reflectance, Rrs, and the particulate absorption and backscattering coefficients, a_p and b_{bp}, is given by:

$$Rhow = \gamma \frac{b_{bnp} + b_{bp}}{a_{np} + a_p + b_{bnp} + b_{bp}}$$

where $\gamma = \Re \frac{f\pi}{Q}$ [sr^{-1}] accounts for: f a dimensionless factor (Morel and Gentili 1991), $\Re$ the reflection and refraction effects at the surface of water (Morel and Gentili 1996) and Q the ratio of upwelling irradiance to upwelling radiance just below the water surface; a_{np} and b_{bnp} are the non-particulate absorption and backscattering coefficients and a_p and b_{bp} are the particulate absorption and backscattering coefficients. The model assumes linear relationships between b_{bp} and turbidity, T, and between a_p and T through turbidity-specific absorption, a^*_{pT} , and backscattering, b^*_{bpT} , coefficients (i.e. $a_p = a^*_{pT} \times T, b_{bp} = b^*_{bpT} \times T$), and also$b_{bnp} = 0$. This leads to the formulation of the algorithm as:

$$T = A \frac{Rhow}{1 - Rhow/C}$$

Where $A = \frac{a_{np}}{\gamma b^*_{bpT}}$ and C= $\gamma \frac{b^*_{bpT}}{a^*_{pT} + b^*_{bpT}}$.

The coefficient C is estimated from literature since uncertainty in C has no significant impact on the model which is used in the linear regime, i.e. $Rhow \ll C$. The coefficient A is calibrated using *in situ*

[4] this is a narrow band parameter, as defined in section 5.5

measurements of reflectance and turbidity. That algorithm has been tested in various waters around the world (Gironde River in France, Scheldt River in Belgium, Río de la Plata in Argentina) showing a quite universal relationship for these waters, when using MODIS near infrared band 859 nm (Dogliotti et al. 2015).

Turbidity measurements from 2007 up to 2013 were collected in various waters, including the Southern North Sea, French Guyana coastal waters and the Mediterranean Sea (described in Neukermans et al., 2012), measurements from three pontoons: in the Scheldt (Belgium), in Río de la Plata (Argentina) and the Gironde Rivers (France) as described in (Dogliotti et al. 2015). This dataset was extended here by recent turbidity and reflectance measurements from three RV Belgica campaigns, carried out in April and July 2014 and in April 2015, in the Southern North Sea and the Scheldt Estuary. The protocol for turbidity and for reflectance measurement during 2014 and 2015 campaigns is identical to that followed by RBINS in the previous campaigns.

From the initial set of 329 reflectance spectra, 161 were simultaneously collected with turbidity samples, and in stable sky conditions (where the variability of Lsky(750 nm) didn't exceed 10% at each station). This dataset is further split into two datasets: one subset of *N* =43 measurements collected from 2007 up to 2010 is used to calibrate the turbidity algorithm and the other subset of N_v = 118 measurements (from 2011 up to April 2015) is used to validate the calibration coefficients.

Type II linear regression analysis are performed on the independent variables T and the transformed variable $= \frac{Rhow}{1-Rhow/C}$, yielding the best curve fitting the *in situ* measurements, plotted in Figure 15.

The results of the regression analysis show the highest coefficient of determination R^2=96.8% obtained for band 785 nm based T-algorithm, where the linear relationship covers the full range of turbidity measurements from the four sites (Southern North Sea, the Mediterranean Sea, French Guyana and the Scheldt Estuary). Both SEVIRI bands HRV and the narrow band 640 nm approach the saturation limit (C~0.18) and clearly depict a non-linear regime for turbidity > 30 FNU.

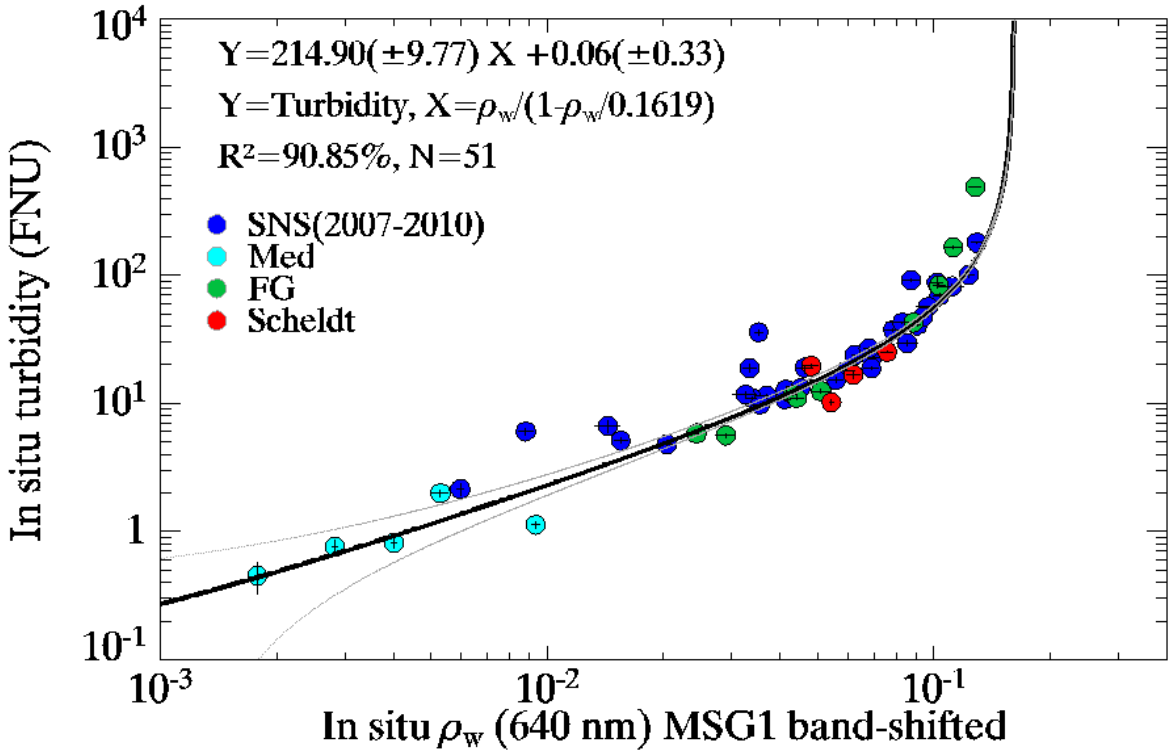
Y=214.90(±9.77) X +0.06(±0.33)
Y=Turbidity, X=ρw/(1-ρw/0.1619)
R²=90.85%, N=51
SNS(2007-2010)
Med
FG
Scheldt
In situ turbidity (FNU)
In situ ρw (640 nm) MSG1 band-shifted

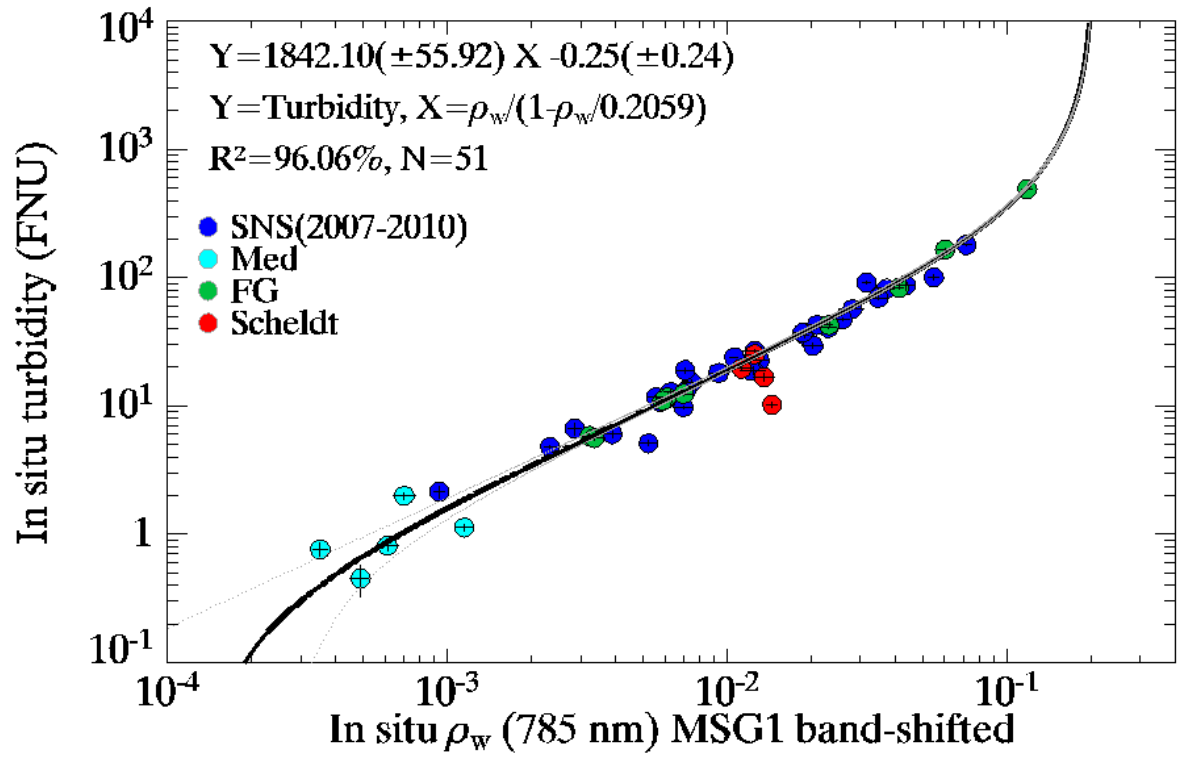
Y=1842.10(±55.92) X -0.25(±0.24)
Y=Turbidity, X=ρw/(1-ρw/0.2059)
R²=96.06%, N=51
SNS(2007-2010)
Med
FG
Scheldt
In situ turbidity (FNU)
In situ ρw (785 nm) MSG1 band-shifted

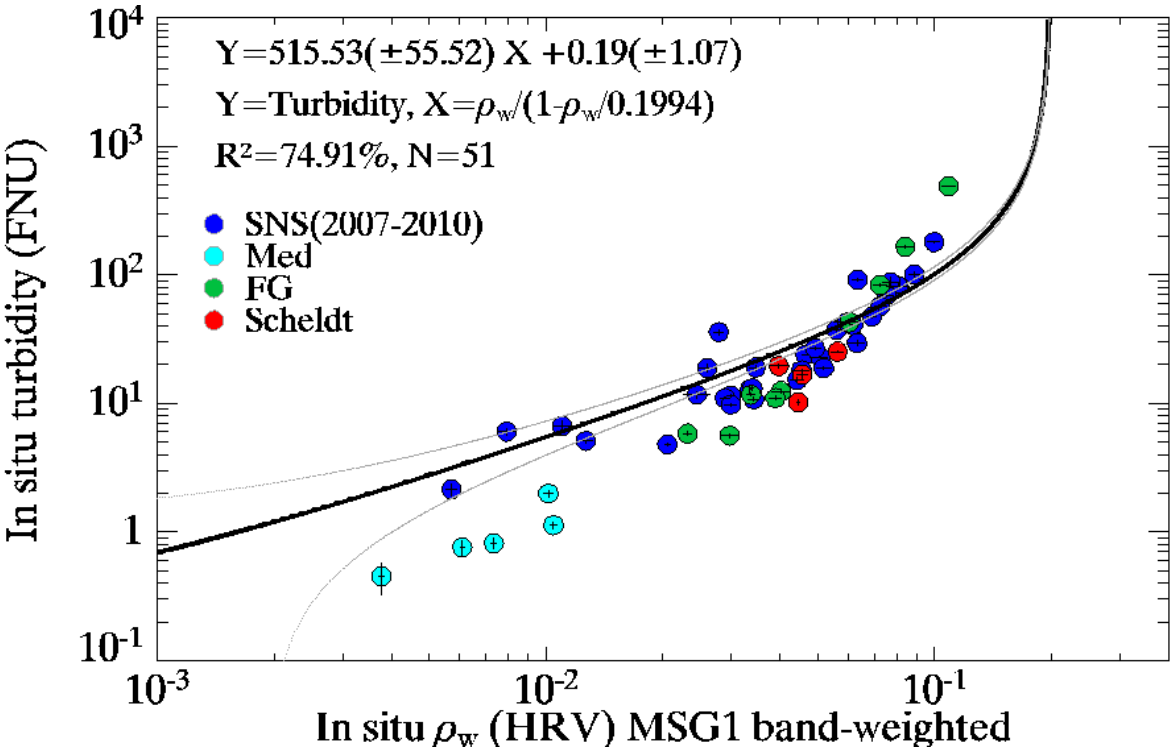

Figure 15: Non-linear regression curves, with best fit to in situ measurements of turbidity and reflectance at the two standard narrow bands 640nm, 785nm and at the MSG1 band-weighted HRV band.

If the model used for the turbid water atmospheric correction is itself based on this Turbidity algorithm then the products derived from Rrs640 and Rrs785 may be identical. In this case, the switching algorithm has no added value. However, the switching algorithm formulation may be useful in case independent methods are used to derive Rrs640 and Rrs785. Since the SEVIRI-WT processor may be run with various options for the turbid water atmospheric correction, it is suggested to use input from the single Rrs785 product, although a formulation switching between Rrs640 and Rrs785 might be advantageous in the future if the non-linear turbid water atmospheric correction ("Method 2") is not adopted as standard.

T-algo coefficients	**SEVIRI band-shift**	
Wavelength(nm)	640	785
A_T	214.9	1842.1
(B_T)	0.06	-0.25
C_T	0.16187	0.20585
R^2	90.9	96.1

Table 5 Coefficients required for applied the Turbidity algorithm to band-shited SEVIRI wavelengths, together with regression offset (B) and correlation coefficient (r^2).

The offset, B, found in the regression analysis of Table 5 is small and likely related to the in situ measurement errors. It is neglected in the SEVIRI turbidity algorithm.

In summary, and writing now for Rrs instead of Rhow with coefficients Ars and Crs for the Rrs algorithm, the T algorithm to be used for the processor is given by:

$$T = Ars785 \frac{Rrs785}{1 - Rrs785/Crs785}$$

where $Ars785 = 1842.1 * \pi$ and $Crs785 = 0.2059/\pi$. To avoid confusion between coefficients used for Rhow or Rrs algorithm variants, it is convenient to remember that C or Crs are respectively the maximum possible water reflectance (Rhow) and Remote sensing reflectance (Rrs) respectively according to this model.

For $Rrs785 > Crs785$, conditions are outside the scope of this model and no value can be recorded for turbidity. For $Rrs785 < 0$ it is likely that sensor noise is giving out of scope conditions and the true turbidity is positive but below the detection limit of the sensor and the algorithm.

8.1.2 T Algorithm for HRV band

The T algorithm described in section 8.1.1 can equally be applied to Rrs785 products derived for the HRV grid as described in section 7.

8.1.3 T Algorithm validation

To validate these models, the calibration coefficients are applied to the reflectance measurements within the validation dataset, yielding the modelled turbidity, $\widehat{T}_i$ at each station *i*, which are then compared to the *in situ* T_i . The mean absolute percentage error, MAPE, and the root mean squared error, RMSE, are computed for each model following:

$$MAPE = \frac{1}{N_v}\sum_{i=1}^{N_v} |T_i - \widehat{T}_i|/T_i \, , RMSE = \sqrt{\frac{\sum_{i=1}^{N_v}(T_i - \widehat{T}_i)^2}{N_v}}$$

The band 785 nm-based T algorithm gives the lowest MAPE=32.5% (Figure 16), while the algorithms using the narrow band 640 nm and SEVIRI HRV give larger MAPE (> 59%). This is mainly due to the sensitivity of these bands to variations in the CDOM and specific particles absorption (Dogliotti et al. 2015). Note that the low RMSE computed for band 640 nm does not take into account unrealistic values obtained for the extremely turbid waters of the Gironde (Rrs approaching Crs), which were rejected for this algorithm, while the extreme values of turbidity in the Gironde could be retrieved by the T-HRV band algorithm.

In conclusion, it is recommended to retrieve turbidity from SEVIRI reflectance at band V0.8µm shifted to the narrow band 785 nm, since the natural variability of specific absorption (CDOM, particles) may hugely impact reflectance at the narrow band 640 nm and at SEVIRI HRV band.

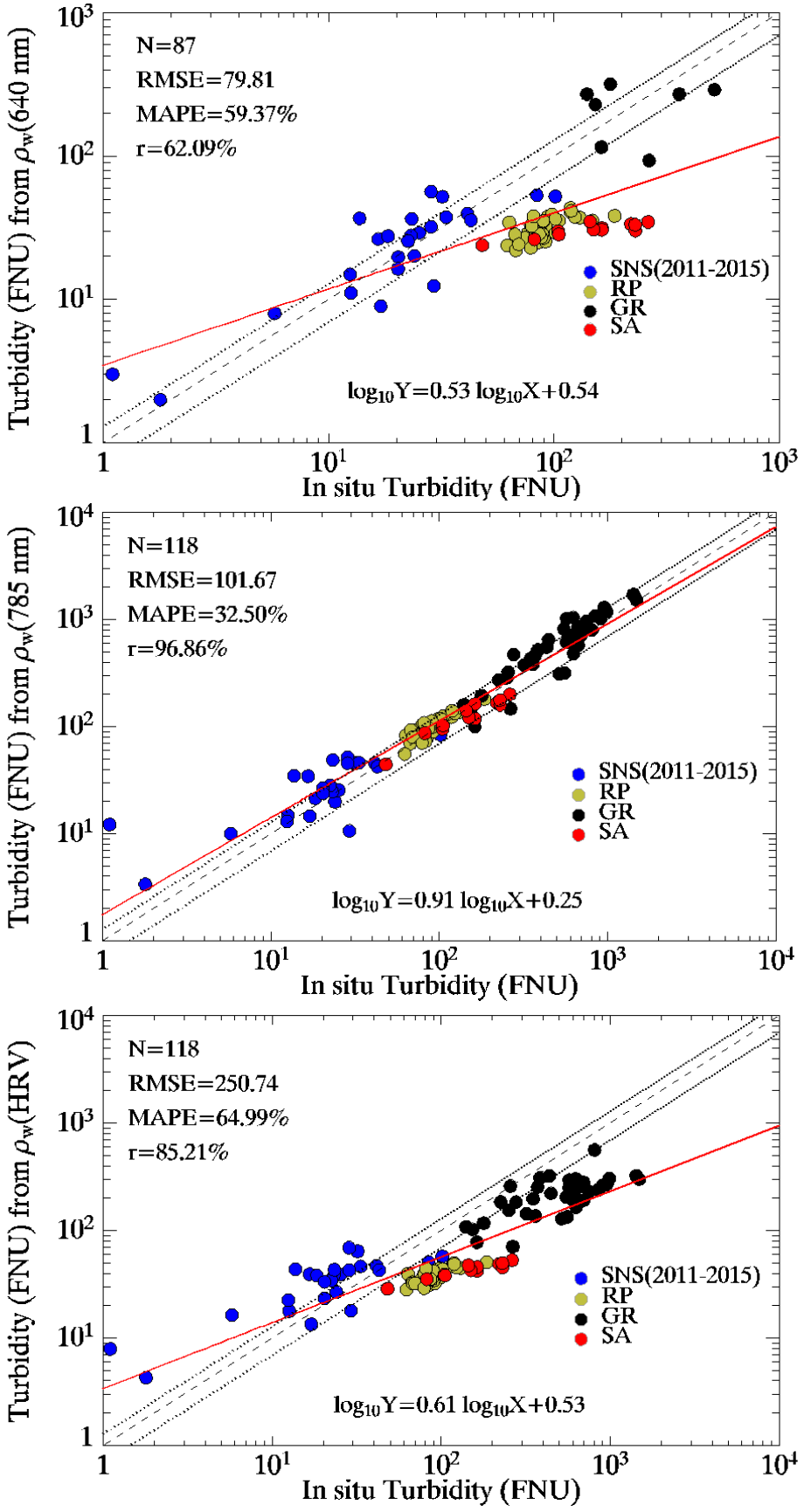

Figure 16: Modelled versus measured turbidity using the narrow band 640 nm (upper figure), 785 nm (middle) and SEVIRI HRV band. The dashed line is the 1:1 line, the dotted lines are the +/-30% around the 1:1 line, and the red line is the linear regression between the in situ and the modelled data.

8.1.4 T Uncertainties

It is expected that the main source of uncertainty for T will be from the reflectance input. The T uncertainty can then be estimated directly as:

$$\Delta T = Ars785 \frac{1}{\left(1 - \Delta Rrs785/Crs785\right)^2}$$

8.1.5 T Quality flagging

Quality flagging for T would typically involve propagation of any poor quality flagging of the input Rrs785 product.

8.1.6 T algorithm adaptation to different SEVIRI sensors

The algorithm of section 8.1.1 applies to the standard Rrs products of all SEVIRI sensors. Differences in the spectral response functions over different sensors are accounted for when deducing the narrowband Rrs640 and Rrs785 products from the band-weighted ρ_w intermediate products.

8.1.7 T algorithm limitations and recommendations for future improvements

The current T algorithm assumes that the non-linear turbid water model will be used for atmospheric correction. If a linear is used then it might be necessary to improve the T algorithm for clearer waters by use of the Rrs640 product, possibly using a weighted algorithm based on both Rrs640 and Rrs785 products.

8.2 Suspended Particulate Matter (SPM)

As noted in the Product Definition Document (D1.2), suspended particulate matter (SPM) is defined the dry mass concentration of particles suspended in a volume of water.

8.2.1 SPM Algorithm description

Whereas the early work of (G. Neukermans et al. 2009) estimated SPM directly from reflectance, the approach adopted here is to estimate SPM from the master optical product, T, as proposed by (Dogliotti et al. 2015). Most data and theory suggest that SPM can be linearly related to T .

A recent study of SPM and T data has been carried out within the FP7/HIGHROC project (Nechad, unpublished)using data from many regions (Southern North Sea, Scheldt Estuary, Gironde estuary, Rhône plume, Baie de Bourgneuf, French Guyana, La Plata estuary, Western Mediterranean, port of Zeebrugge, etc.). This study suggests that inter-region variability of SPM/T is quite low and a general conversion can be achieved using:

$$SPM = 0.90 * T$$

If there is specific knowledge of a different SPM:T ratio for a certain region, then a local SPM product can easily be derived by a user by postprocessing (Doerffer 2006) the standard T product obtained with default SPM:T.

8.2.2 SPM Algorithm for HRV band

The SPM algorithm described in section 8.2.1 can equally be applied to T products derived for the HRV grid as described in section 7.

8.2.3 SPM Algorithm validation

SPM algorithm validation should be made using for example RBINS seaborne reflectance and SPM data.

8.2.4 SPM Uncertainties

The SPM product will contain the uncertinaty of the T product plus an additional uncertainty related to the natural variability of SPM/T. The latter is estimated as 14% on the basis of the HIGHROC datasets. Net uncertainty for SPM is then:

$$\frac{\Delta SPM}{SPM} = \sqrt{\left(\frac{\Delta T}{T}\right)^2 + 0.14^2}$$

8.2.5 SPM Quality flagging

Quality flagging for SPM would typically involve propagation of any poor quality flagging of the input Rrs785 product.

8.2.6 SPM algorithm adaptation to different SEVIRI sensors

The algorithm of section 8.2.1 applies to the standard T product of all SEVIRI sensors. Differences in the spectral response functions over different sensors are accounted for when deducing the narrowband Rrs640 and Rrs785 products from the band-weighted ρ_w intermediate products.

8.2.7 SPM algorithm limitations and recommendations for future improvements

Limitations and recommendations for improvement of the SPM are essentially the same as for the Rrs products on which it is based.Particulate backscatter (bbp640)

As noted in the Product Definition Document (D1.2), particulate backscatter at 640nm (bbp640) is defined as the angular integral over the backscattering hemisphere (all scattering angles greater than 90°) of the Volume Scattering Function at 640nm.

8.2.8 bbp640 Algorithm description

Particulate backscatter at 640nm is very closely related to turbidity (side-scattering at 860nm) with only very minor natural variability expected because of possible variability in the particulate scattering phase function and the spectral dependency of backscatter.

The data of (G. Neukermans et al. 2012) provides good coverage of many clear and turbid waters and shows very strong correlation between SPM, T and bbp650. Neglecting the slightl wavelength shift (from 650nm to 640nm) their data suggests a relationship:

$$bbp640 = 1.02 * T$$

where the constant of proportionality provides a conversion from FNU to m-1.

8.2.9 bbp640 Algorithm for HRV band

The bbp640 algorithm described in section 8.2.8 can equally be applied to T products derived for the HRV grid as described in section 7.

8.2.10 bbp640 Algorithm validation

There is, at present, insufficient data for bbp640 in very turbid waters to validate this algorithm.

8.2.11 bbp640 Uncertainties

The uncertainty related to natural variability in the conversion from T to bbp640 is very low (but could be calculated precisely for different scattering phase functions where the variability of the phase function is known). The relative uncertainty of bbp640 will thus be estimated to equal the relative uncertainty of T:

$$\frac{\Delta bbp640}{bbp640} = \frac{\Delta T}{T}$$

8.2.12 bbp640 Quality flagging

The Product Confidence Flag will be the same as the Product Confidence Flag for T.

8.2.13 bbp640 algorithm adaptation to different SEVIRI sensors

The algorithm of section 8.2.8 applies to the standard T product of all SEVIRI sensors. Differences in the spectral response functions over different sensors are accounted for when deducing the narrowband Rrs640 and Rrs785 products from the band-weighted ρ_w intermediate products.

8.2.14 bbp640 algorithm limitations and recommendations for future improvements

Limitations and recommendations for improvement of the bbp640 product are essentially the same as for the Rrs products on which it is based.

9 Attenuation-related products (L2W/K)

9.1.1 Diffuse attenuation of PAR

Various definitions of diffuse attenuation coefficient and of Photosynthetically Available Radiation (PAR) are possible.

For example, PAR may be considered in power units (W m^{-2}) or in quantum (photons $m^{-2}s^{-1}$) units, may be integrated over different wavelength ranges and may be evaluated as a spectral integral of downwelling irradiance or of scalar irradiance, taking respectively the cosine-weighted integral of downward radiance or the spherical integral of radiance as defined by [Mobley, 1994]. Since the main user interest is for phytoplankton and primary production applications the definition of PAR proposed for SEVIRI-WT is of quantum scalar irradiance spectrally integrated over the range 400-700nm.

As regards the diffuse attenuation coefficient, this can be defined for different depth ranges. The choice of depth range for attenuation of PAR is particularly critical because KdPAR varies significantly with depth, even for a homogeneous water column and cloudy sky (diffuse illumination), because of the rapid attenuation of red light in the upper few metres [Lee, 2009]. For compatibility with the euphotic depth parameter it is proposed here to evaluate KdPAR for the depth range down to the euphotic depth.

The SEVIRI algorithm of (G. Neukermans, Ruddick, and Greenwood 2012), based on measurements by (Devlin et al. 2008), will be used here after adaptation to the T product used. Thus KdPAR in m-1 is estimated from:

$$KdPAR = 0.325 + 0.066 * 0.90 * T$$

Tests (not shown) suggest that while this algorithm performs well for high T, performance at low T is less satisfactory with strong overestimation of KdPAR for the clearest waters arising from the large coefficient 0.325 m-1.

9.1.2 Euphotic depth

The euphotic depth is defined as the depth where the quantum scalar irradiance reaches 1% of its value just beneath the water surface. Thus, by definition:

$$z_e = \frac{ln100}{KdPAR}$$

9.1.3 Secchi depth

The Secchi depth is the depth at which a black and white disk of diameter 30cm, lowered by rope into water without shadow (thus on the sunny side of a ship for shipborne measurements), disappears from the view of a human observer.

In addition to the obviously subjective nature of human observers, this parameter is not well-defined and will obviously vary according to many factors including cloud cover, sun zenith angle, sea state, etc. [Preisendorfer, 1985]. It is noted also that many historical measurements use different equipment, e.g. a white disk or a disk of different diameter. However, since Secchi depth is a parameter still used and required by many users (see the SEVIRI-WT URD), it is retained here. As for the other attenuation-related products the poor spectral content of SEVIRI does not allow good representation of attenuation except in turbid waters. The formulation of (Devlin et al. 2008) is adopted here:

$$SD = \left(\frac{e^{-0.01}}{KdPAR} \right)^{1/0.861}$$

The Secchi Depth product will obviously suffer the same limitations at the KdPAR product.

10 Other L2W flag products

10.1.1 Coccolithophore bloom flag

The definition of this parameter is not yet clear and will need to be refined after the Scientific Development Task B. This parameter should in some way indicate the presence of coccolithophores. An objective scientific definition could perhaps be developed from an estimate of the concentration of coccoliths compared to a suitable threshold value. The latter threshold will depend on region, according to whether coccolithophore are known to potentially exist or known to never exist. The latter allows to avoid incorrect flagging in turbid waters, but requires more analysis of SEVIRI data in the full disk for adequate definition.

10.1.2 Extreme high biomass bloom flag

The definition and even the feasibility of this parameter is not yet clear and will need to be refined after the Scientific Development Task B. This parameter should in some way indicate the presence of an extreme high biomass algal bloom (as distinct from high backscatter from non-algae particles). An objective scientific definition could perhaps be developed from an estimate of the particulate backscatter of algal particles (excluding non-algal particles) compared to a suitable threshold value. This is probably best achieved via multitemporal analysis of SEVIRI full disk data in specific regions, but requires more analysis of SEVIRI data in the full disk for adequate definition.

10.1.3 Extreme cyanobacteria bloom or surface scum flag

The definition and even the feasibility of this parameter is not yet clear and will need to be refined after the Scientific Development Task B. This parameter should in some way indicate the presence of an extreme high biomass cyanobacteria bloom (as distinct from high backscatter from non-algae particles) or a surface scum. An objective scientific definition could perhaps be developed from an estimate of the reflectance in the Short Wave Infrared band. This is probably best achieved via multitemporal analysis of SEVIRI full disk data in specific regions, but requires more analysis of SEVIRI data in the full disk for adequate definition. In particular, it will be necessary to choose carefully (or temporarily turn off) the pixeld identification for water/non-water since high SWIR reflectance will occur for all non-water pixels, including (permanent) land, clouds and floating vegetation/scum.

11 Conclusions and Recommendations

The present document provides the basis for algorithms to be implemented in the SEVIRI-WT processor.

The atmospheric is by far the most complex algorithm and is on the critical path of the project. Full details are given here, including new work on how the full disk will be segmented for aerosol type determination, on the turbid water model for aerosol correction using a non-linear analytical water reflectance model, possible use of the NIR1.6 band, adaptation of all LUT to different MSG platforms, refinement of approach for using the HRV to achieve higher resolution and a new methodology for standardisation of wavelength across different MSG platforms ("band shifting").

The band shifting analysis concludes that output should be provided for narrow bands at 640nm and 785nm, where the latter is quite different from the SEVIRI central wavelength because of the asymmetry of the water reflectance around the central wavelength.

Recalibration and revalidation of the turbidity algorithm is provided here as well as a new methodology and calibration for interrelating the other L2W/S products (SPM, bbp640) to the "master" turbidity product. L2W/K algorithms are defined, again as function of turbidity.

A conceptual outline for some L2 flags is given, but full scientific definition requires more analysis of the full disk processor output. Since the latter will be rather simple, perhaps one-line, functions of the Rrs640 and Rrs785 products they can be easily implemented in the processor later or via post-processing of the level 2 data.

Annex A Semi-analytical reflectance model

The turbid water component of the atmospheric correction algorithm, the HRV-sharpening algorithm and the L2W/S retrieval algorithms all require a model to relate reflectance to inherent optical properties (IOP), typically defined via the total spectral absorption coefficient and total volume scattering function. The Hydrolight 5.1 radiative transfer model is generally accepted as the most accurate model to calculate directional reflectance from IOPs, although its validity obviously depends on the validity of the IOP inputs and models used. In the SEVIRI context there are only two spectral bands (0.6µm and 0.8µm) with non-zero water reflectance and their dependence on IOPs is rather simple: the total spectral absorption coefficient is largely determined by pure water absorption and, to a lesser extent, non-algal particulate absorption and the total spectral volume scattering function is largely determined by particulate scattering. There is, thus, essentially only one degree of freedom, which can be represented by an IOP relating to particulate (back)scattering. In this context a suitably calibrated semi-analytical reflectance model can give very good performance and has the advantage over Hydrolight of giving easily understandable, programmable and verifiable algorithms and uncertainty estimates. It is therefore proposed here to use as SEVIRI-WT reflectance model the formulation of (Nechad, Ruddick, and Park 2010), which is based on the semi-analytical reflectance model of (Gordon et al. 1988) with additional approximations and IOP models as described in full in section 2 of that paper.

The (Nechad, Ruddick, and Park 2010) model can be used with any single parameter which is linearly correlated to particulate scattering and absorption, e.g. Turbidity (side-scattering at 860nm), particulate backscatter at a single wavelength, Suspended Particulate Matter concentration, etc. It is written here as function of turbidity for reasons explained in detail in section 8. Thus

for any narrow or broad band reflectance as:

$$T = A_{T(\lambda)} \frac{\rho_{w(\lambda)}}{1 - \rho_{w(\lambda)}/C_{(\lambda)}}$$

where λ represents wavelength. The inverse algorithm to estimate reflectance from turbidity is then:

$$\rho_{w(\lambda)} = \frac{T}{\left(A_{T(\lambda)} + T/C_{(\lambda)}\right)}$$

This model allows to easily and consistently relate reflectance at two different wavelengths, ρ_{w1} and ρ_{w2} via:

$$\rho_{w1} = \rho_{w2} \frac{A_{T2}}{A_{T1} + \rho_{w2}\left(A_{T2}/C_1 - A_{T1}/C_2\right)}$$

In the low reflectance limit the model gives $\rho_{w(\lambda)} = T/A_{T(\lambda)}$ and $\rho_{w1} = \rho_{w2}\, A_{T2}/A_{T1}$.

In the high reflectance limit the model gives $\rho_{w(\lambda)} \to C_{(\lambda)}$ as $T \to \infty$.